5-2010

Upgrade To The Pierre Auger Cosmic Ray Observatory's Lidar System

Emily B. Petermann
University of Nebraska at Lincoln, empetermann@gmail.com

Petermann, Emily B., "Upgrade To The Pierre Auger Cosmic Ray Observatory's Lidar System" (2010). *Theses, Dissertations, and Student Research: Department of Physics and Astronomy*. 10.
http://digitalcommons.unl.edu/physicsdiss/10

UPGRADE TO THE PIERRE AUGER COMSIC RAY OBSERVATORY'S LIDAR SYSTEM

by

Emily B. Petermann

A THESIS

Presented to the Faculty of
The Graduate College at the University of Nebraska
In Partial Fulfillment of Requirements
For the Degree of Master of Science

Major: Physics and Astronomy

Under the Supervision of Professor Gregory Snow

Lincoln, Nebraska

May, 2010

UPGRADE TO THE PIERRE AUGER COMSIC RAY

OBSERVATORY'S LIDAR SYSTEM

Emily Brooke Petermann, M.S.

University of Nebraska, 2010

Advisor: Gregory Snow

The Pierre Auger Cosmic Ray Observatory currently operates four elastic lidar systems in order to characterize the atmospheric aerosol content above the observatory. The atmospheric information gained by the lidar system is then used in the calibration of the observatory's four fluorescence detectors. Currently the four lidars in operation are unable to accurately determine the aerosol content below a distance of 1 km. A project is currently underway to upgrade the current lidar system by adding an additional detector to each of the existing lidar systems. The considered designs for this upgrade and the initial results from the upgrade prototype are the subject of this thesis.

Contents

Introduction

The Pierre Auger Cosmic Ray Observatory uses two techniques to observe extensive air showers caused by ultra high-energy cosmic rays interacting with the molecules in the upper atmosphere [13]. The first technique is to observe a portion of the secondary particles that make up the air shower using surface detectors that are spread out on the ground over approximately 3000 km^2. The second technique uses fluorescence detectors located around the perimeter of the array. These detectors observe the fluorescence light generated by the secondary particles of the air shower when they interact with the atmosphere above the surface detectors.

For the Pierre Auger Observatory the atmosphere acts as both a calorimeter, in which the showers develop, and an attenuating medium that both absorbs and scatters the fluorescence light generated by the air showers [17]. The properties of the atmosphere must be well known in order to obtain accurate information about the shower and thus accurate information about the properties of the primary cosmic ray particle that caused the shower. To determine the properties of the atmosphere the Pierre Auger Observatory has an extensive atmospheric monitoring program.

My thesis begins with a brief overview of cosmic ray physics and an introduction to the Pierre Auger Observatory with an overview of the atmospheric monitoring program (Chapters 1 and 2).

One of the main components of the Pierre Auger Observatory's atmospheric monitoring program is a lidar system. Lidar stands for light detection and ranging. Chapter 3 will give an introduction to lidar theory. Then the current lidar system used by the Pierre Auger Observatory will be described. The current lidar system in use by the Pierre Auger Observatory is unable to accurately detect the composition of the atmosphere below a range of 1 km from the lidar. The main topic of this thesis is the work done to design an upgrade to the current lidar system. This upgrade will improve the accuracy of the lidar system in the range of less than 1 km. In chapter 3 the considered designs for the upgrade will be described. Finally, the preliminary results of the first prototype of the chosen design will be shown.

Chapter 4 will briefly summarize what was learned from the prototype and what work still needs to be done in order to incorporate the upgrade into the current lidar system.

Chapter 1
Cosmic Ray Physics

The discovery of cosmic rays occurred over a hundred years ago. At the end of the nineteenth century British physicist Charles Wilson carried out a series of experiments in static electricity. In these experiments he measured how quickly charge leaked away from a gold leaf electroscope [4]. In an effort to determine the cause of the loss of charge in the electroscope Wilson enclosed the apparatus in a sealable container and varied the source of air in the apparatus. He found that the type of air, polluted air from the city or cleaner air from the countryside, had no effect on the leakage of charge [18]. Next he performed the experiments comparing the rate of leakage of charge in both the daylight and in the dark and found no effect. He also found that there was no difference in the leakage rate whether the electroscope was positively or negatively charged. He determined that somehow the air in the container was being ionized with an equal number of positive and negative charges [18]. In 1901, Wilson postulated that the source ionization could be radioactive rays from outside the Earth’s atmosphere [4]. In order to test this theory Wilson performed tests underground; unfortunately he did not realize that radioactivity in the earth would also contribute to the leakage rate of the charge and his equipment was not capable of separating the effects. This led him to conclude that the ionization must be a property of the air itself. It was another decade before the source of the ionization was proven to be the result of cosmic radiation.

On 7 August 1912 Victor Hess flew in the gondola of a hydrogen balloon to an altitude of 5350 meters [4]. On both the ascent and decent Hess measured the ionization levels using an ionization chamber designed by Father Thomas Wulf. Hess found that as the altitude increased there was an initial drop in the ionization, however at an altitude greater than 2000 meters the ionization level began to rise with a sharp increase as the maximum altitude was reached [14]. Hess concluded that below 2000 meters the ionization of the air was caused by terrestrial radiation sources and for higher altitudes the ionization was caused by a source outside the Earth's atmosphere. By 1925 it was agreed by most that the source of the ionization phenomena was extra-terrestrial in origin and American physicist R.A Millikan coined the name cosmic rays to describe the radiation responsible for the ionization [14].

In the following decades a great deal of progress was made towards understanding cosmic rays. In 1939 Pierre Auger discovered extensive air showers, a process in which a primary cosmic ray particle interacts with the atoms in Earth's atmosphere setting off a cascade of secondary particles. From the 1930s to the early 1950s most new particle discoveries were found due to studies in cosmic ray interactions. At the time the energies of cosmic ray interactions were far greater than those that could be achieved in a laboratory. In the 1970s several theories about the acceleration mechanisms of cosmic rays were developed.

In recent decades attention has turned to ultra high-energy cosmic rays (UHECR). These particles have energies of 10^{19} to 10^{20} eV. These energies are several orders of magnitude greater than anything produced by manmade experiments to date. By studying UHECR the hope is to answer the remaining questions about cosmic ray particles' origins and nature.

1.1 Main Characteristics of Cosmic Rays

1.1.1 Energy Spectrum

The cosmic ray spectrum ranges in energy from 10^6 eV to 10^{20} eV (see Figure 1.1) and over this range the flux changes by about thirty orders of magnitude. The cosmic ray spectrum follows an approximate power law of the form $\mathrm{E}^{-\alpha}$. On the whole the cosmic ray energy spectrum does not change its structure much, however there are some important features that should be noted. First of all, at low energies, below 10^9 eV, cosmic rays are difficult if not impossible to detect due to the fact that the magnetized solar winds from the Sun impedes their approach [4]. The next important feature is known as the *knee*; it is located at approximately 10^{15} eV. It is at this energy the cosmic ray spectrum steepens. The third feature of note is known as the *ankle,* which occurs at energies of about 10^{18} eV; here the cosmic ray energy spectrum flattens again. The last feature in the cosmic ray spectrum is the Gresien, Zatsepin and Kuzmin (GZK) cutoff, which should occur at about 10^{20} eV [16].

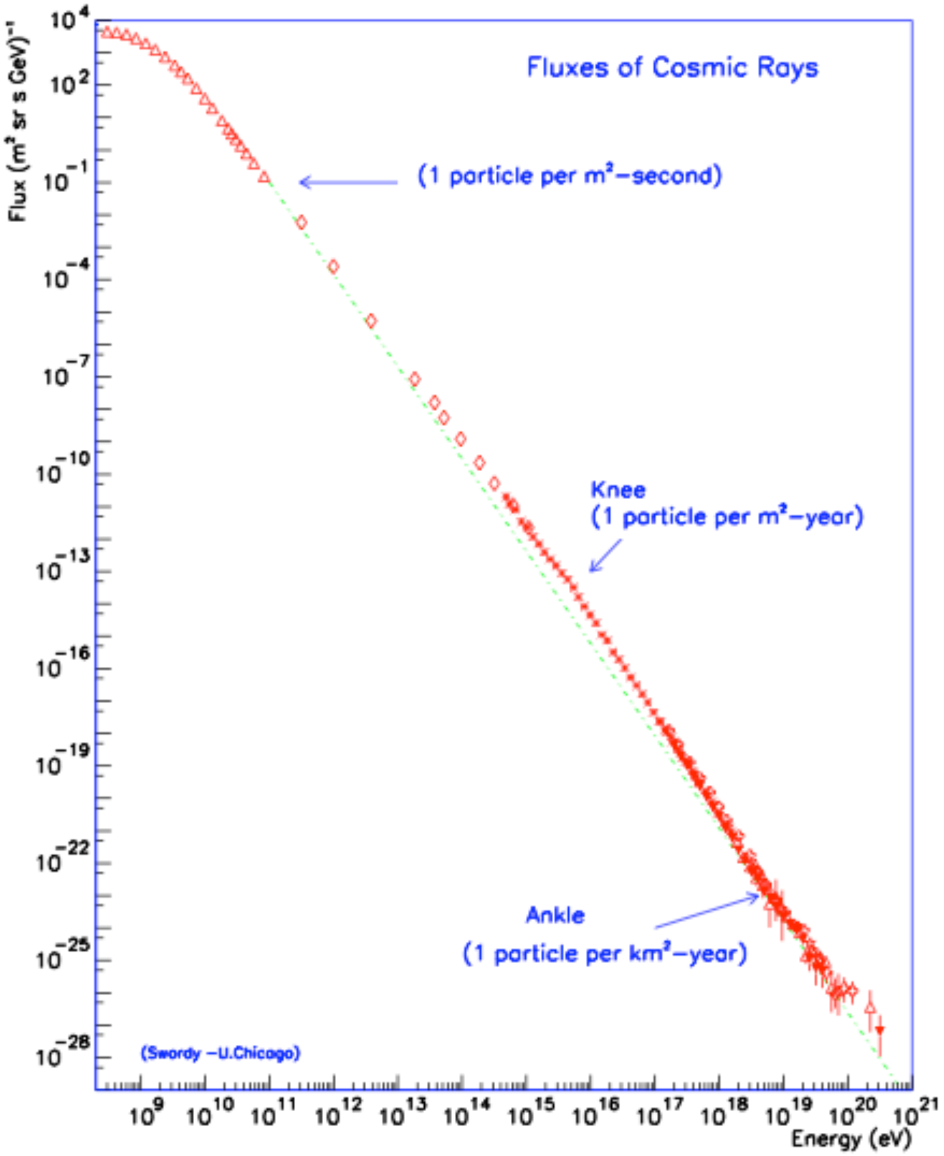

Figure 1.1: Cosmic Ray Spectrum.

A year after the discovery of the cosmic microwave background (CMB) in 1965, Gresien, Zatsepin and Kuzmin predicted that cosmic ray protons with energies exceeding about 6×10^{19} eV would interact with the CMB, losing a significant fraction of their energy [4]. These interactions would cut off the cosmic ray spectrum preventing the high-energy particles from surviving the propagation to reach Earth.

1.2 The Origin of Ultra High Energy Cosmic Rays

The source of the highest energy cosmic rays is currently unknown. However, there are several requirements for possible sources. To begin with, the source of these cosmic rays must be relatively close or energy losses during propagation would imply the sources have extremely large luminosities. Also, the maximum energy of a cosmic ray and the main features of an acceleration site, radio galaxies, pulsars, etc, are given by the following relation

$$E_{max} = \gamma eZBR\,,$$

where B is the magnetic field strength of the acceleration site, R is the linear dimension of the acceleration site, eZ is the charge of the accelerated particle and γ is the Lorentz factor [13]. These requirements limit the possible sources of ultra high-energy cosmic rays.

1.2.1 Possible Astrophysical Sources of UHECR

There are several possible candidates for ultra high-energy cosmic ray sources. In this section some of the most probable sources are briefly described.

Radio Galaxies

One of the most attractive candidates for ultra high-energy cosmic rays is radio galaxies. The particular type of radio galaxy that is favored is a Fanaroff-Riley II type galaxy, which exhibits two jets going in opposite directions. These jets produce a termination shock in the extragalactic medium that is known as a hot spot. The hot spot may contain magnetic fields exceeding 10 μG. It has been estimated that protons could be accelerated to about 10^{21} eV in these areas.

Gamma Ray Bursts

The exact cause of gamma ray bursts is still unknown, however the observable effects are believed to be due to the dissipation of the kinetic energy of a relativistically expanding wind. Although the exact cause of gamma ray bursts is currently unknown they are still considered possible candidates for ultra high-energy cosmic ray sources.

Colliding Galaxies

The collision of galaxies, as well as the movement of galaxies through clusters, produces large shocks visible in the radio frequencies. A large enough shock could potentially provide accelerations to above 10^{20} eV.

Pulsars

Pulsars are the smallest known objects that could accelerate cosmic rays to ultra high energies. Unlike the previous sources pulsars would utilize direct acceleration as opposed to acceleration due to shock waves [16]. The two properties of pulsars that make them attractive candidates for cosmic ray sources are the pulsar's extremely fast rotation and its large magnetic field. Theory suggests that the rotation and magnetic field produce an electric current at the surface of the pulsar that accelerates electrons and protons to high speeds before launching them into space [4].

Active Galactic Nuclei

Active Galaxies are believed to be supermassive black holes surrounded by an accretion disk. This disk is composed of hot gas from stars that have been torn apart by the tidal forces produced by the black hole. These black holes emit beams of high-energy particles perpendicular to the accretion disk. On 9 November 2007 the Pierre Auger Collaboration released results showing a correlation between the arrival directions of cosmic rays with an energy exceeding 6×10^{19} eV and active galactic nuclei positions [10].

Chapter 2
The Pierre Auger Observatory

2.1 The Auger Project

Jim Cronin and Alan Watson conceived the Pierre Auger Observatory in 1995. This observatory has three main features that make it ideal for examining high-energy cosmic rays. The first feature is the full sky coverage by the observatory [13]. This full sky coverage will be achieved by having two sites, one to cover the southern hemisphere and another to cover the northern hemisphere. The southern hemisphere site is fully operational and currently taking data, the northern site is, at present, in the planning stages. Having full sky coverage is important for confirmation of cosmic ray sources.

The second main feature of the observatory is the large detector area [13]. The southern site has a detector area of 3000 km^2. This large detector area allows the detector to focus on the highest energy cosmic rays. The current plan calls for the northern site to be larger than the southern site [12]. The increase in size is done in order to focus on just the highest energy cosmic rays.

The third feature is the fact that the Pierre Auger Observatory uses a hybrid technique [13]. This hybrid technique includes both a surface array of Cherenkov detectors and a system of fluorescence detectors that observe the light caused by the cosmic ray shower particles interacting with the atmosphere.

The following sections will give a brief overview of the Pierre Auger Observatory, the detectors currently used for cosmic ray detection and the atmospheric monitoring program used for the calibration of the cosmic ray detectors. The sections on the atmospheric monitoring will briefly touch on several different atmospheric monitoring devices used by the observatory. For this thesis the most important detector discussed is the lidar system, which will be described in more detail in chapter 3. The lidar system a is component of the atmospheric monitoring program. The work done for this thesis is a study of several possible designs for an upgrade to the existing lidar system and the installation of a prototype upgrade.

2.2 Southern Site

The Pierre Auger Observatory southern site is located in western Argentina near the city of Malargüe. It covers approximately 3000 km^2, Figure 2.1. The observatory measures cosmic ray showers utilizing two detector types [13]. The first type is the Surface Detectors (SDs), which measure the cosmic ray shower at ground level. The second type is the Florescence Detectors (FDs), which observe the cosmic ray shower in the air by monitoring the florescence light caused by the nitrogen molecules in the air being excited by the particles in the cosmic ray shower.

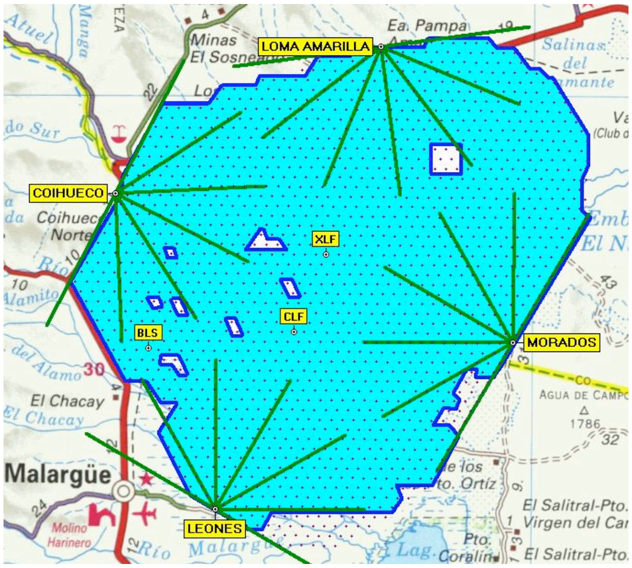

Figure 2.1: Map of the Pierre Auger Cosmic Ray Observatory as of 27 April 2009 [11]. The areas with operational SDs have been shaded in and the four FDs located around the perimeter of the array are labeled in yellow.

2.3 The Northern Site

The Pierre Auger Observatory northern site is currently in the planning stages. The northern site will be located in the southeastern corner of Colorado, in an area covering roughly five counties [12]. The location and planned configuration of the northern site is shown in Figure 2.2.

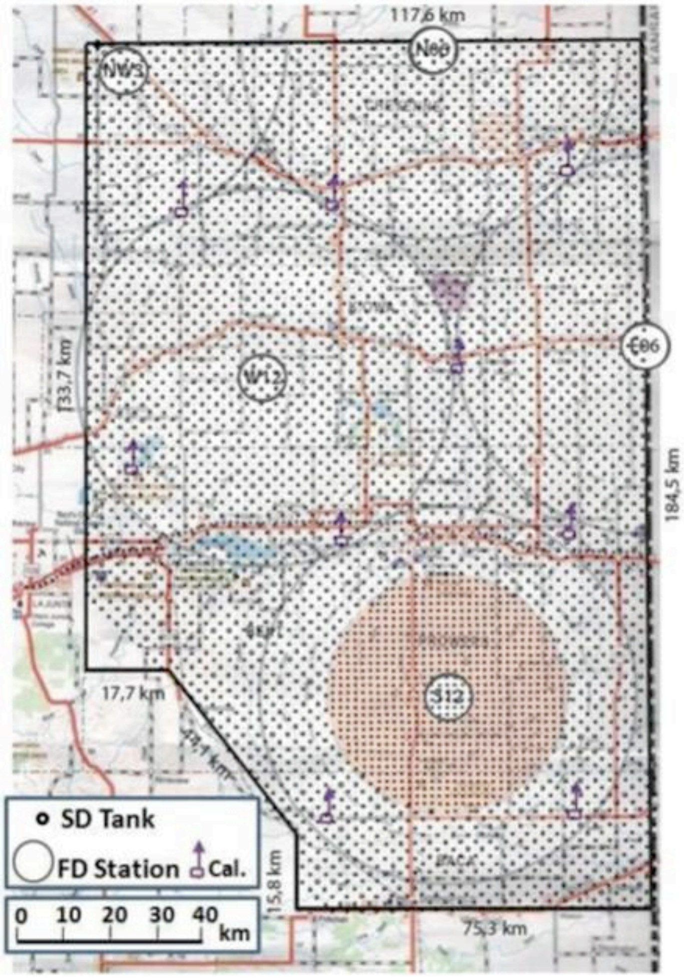

Figure 2.2: Planned configuration of the Pierre Auger Observatory northern site. The smaller dots represent planned SD locations and the five larger circles are FDs [12].

The northern site will differ from the southern site in several ways, the most important being an increase in the size of the surface detector array. This increase in size will focus the northern site on detection of cosmic rays with energy around 10^{20} eV.

2.4 Surface Detectors

The Pierre Auger Observatory southern site is composed of 1600 SDs spaced 1.5 km apart. These SDs are water Cherenkov detectors. Each detector is composed of a cylindrical tank with a height of 1.2 m and a surface of 10 m^2. The detector volume is filled with purified water. Three photomultiplier tubes (PMTs) located at the top of the tank spaced 120º apart observe the interior of the tank. The PMTs in the tank observe the Cherenkov light from emitted from the cosmic ray shower particles as they pass through the purified water. A single SD is shown in Figure 2.3.

Figure 2.3: Surface Detector

2.5 Florescence Detectors

The Pierre Auger Observatory southern site has four FDs, which are located around the perimeter of the array. The names of these four FDs are Los Leones, Los Morados, Loma Amarilla and Coihueco. Each of the FDs is made up of six sub-units called telescopes. These telescopes are composed of an 3.5×3.5 m^2 spherical mirror and a camera made of 440 hexagonal photomultiplier tubes, which act as the pixels of the camera. Additional components such as an ultraviolet filter, which reduces the background light from the night sky, and a diaphragm that reduces spherical spot aberrations, have been installed at all FDs. A diagram of a single FD is shown in Figure 2.4.

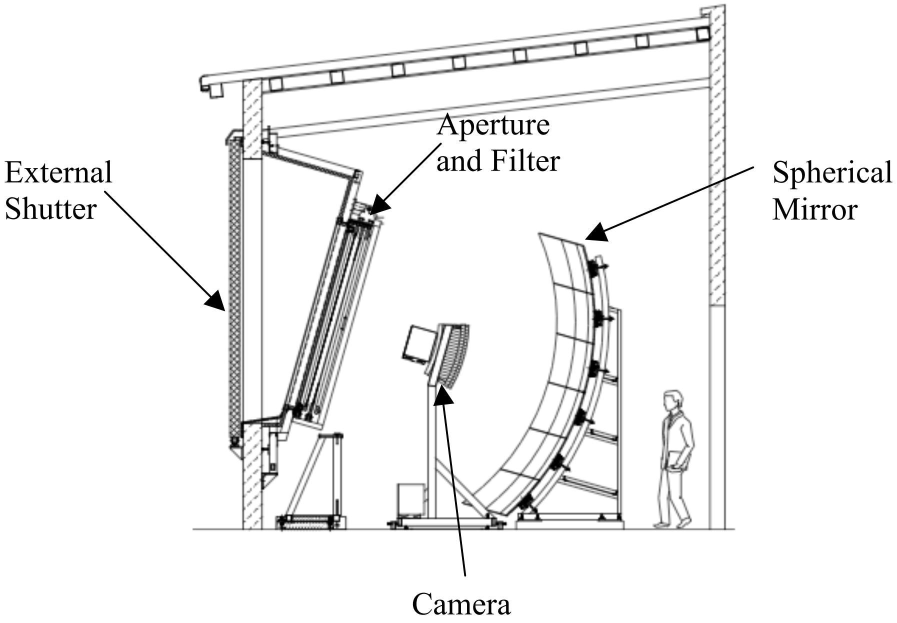

Figure 2.4: Schematic of a single FD showing the main components. [9]

The FD measures the longitudinal profile of a cosmic ray shower by the following process. Fluorescence light produced by the particles in a cosmic ray shower interacting with the nitrogen enters the FD through the window. The external shutter shown in Figure 2.4 covers the window when the FD is not in use. Once the light passes through the window it then passes through a filter and aperture system. This system reduces background and serves as the window protecting the equipment from dust [9]. After the light passes through the filters it is reflected off the mirror and collected by the camera. The camera used in the FD is an actually an array of photomultiplier tubes. A picture of a single FD telescope is shown in Figure 2.5.

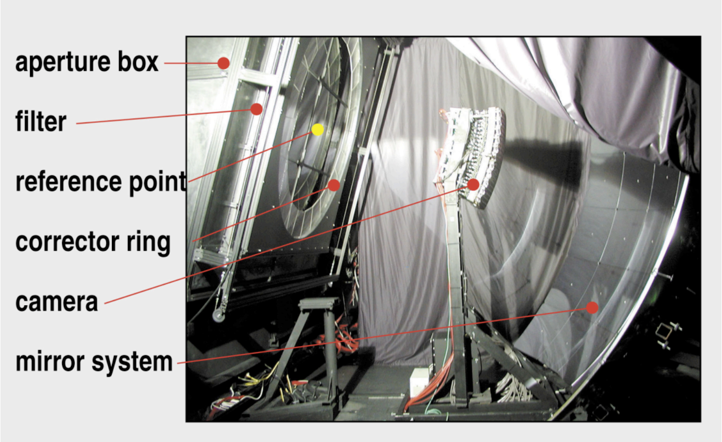

Figure 2.5: Fluorescence Detector telescope [11].

2.6 Atmospheric Monitoring

One of the largest and most important uncertainties in the measurements from the FDs is the estimation of the atmospheric effects on the propagation of the fluorescence light through the atmosphere. In order to reduce this uncertainty the Pierre Auger Observatory uses an extensive atmospheric monitoring system. The devices that make up the atmospheric monitoring system will be described briefly in the following sections.

2.6.1 Balloon Launches Program

In order to determine the average pressure, density and temperature profiles of the atmosphere above the observatory weather balloons are launched periodically from the Balloon Launching Station, BLS, shown in Figure 2.1.

2.6.2 CLF and XLF

The Central Laser Facility, CLF, is located in the approximate center of the array, shown in Figure 2.1. The CLF uses a 355 nm laser to provide a calibrated test beam for the FDs. The CLF provides several calibration measurements for both the FDs and the SDs. The first calibration measurement is the vertical aerosol optical depth as a function of height above the site. The second calibration measurement is the uniformity of the atmosphere horizontally across the site. The third is the timing and the trigger efficiency of the FDs. The final calibration measurement is the timing between the SDs and the FDs. This measurement is done by splitting off a fraction of laser pulses and sending it over a 40 m optical cable to a nearby surface detector [5].

A new laser facility, XFL, was recently installed; this facility is identical to the CLF. The location of the XFL is shown in Figure 2.1.

2.6.3 Weather Stations

The Pierre Auger Observatory utilizes 6 weather stations, one located at each of the four Fluorescence Detector buildings, one located at the central laser facility and a final one located at the Balloon Launch Station. These weather stations monitor the relative ground humidity, temperature, wind velocity, pressure and solar radiance at ground level.

2.6.4 Horizontal Attenuation Monitor

The Horizontal Attenuation Monitor, HAM, is used to study the wavelength dependence of light scattering. This device consists of a light source located at the Coihueco FD building and a receiver located at the Los Leones FD building [3]. During the FDs operation a measurement of the horizontal attenuation length is performed on an hourly basis.

2.6.5 FRAM

The Photometric Robotic Atmospheric Monitor, FRAM, consists of an optical telescope with a CCD camera and a photometer. This device automatically observes a calibration source and a set of stars from which the wavelength dependence of the attenuation and the vertical aerosol optical depth is determined.

2.6.6 Aerosol Phase Function Measurement

The Aerosol Phase Function, APF, light sources are used along with the Fluorescence Detectors to measure the aerosol phase function [3]. There are two APF monitors installed, one at Coihueco and another at Los Morados.

2.6.7 IR Cloud Cameras

An infrared cloud camera is mounted on the roof of each FD building. During data taking these cameras take continuous infrared images of the sky in order to determine cloud presence and shape [3]. The information gained from the IR cameras is then combined with cloud height measurements from the lidar system so that the position of cloud coverage over the site is precisely known. In is extremely essential that the positions of clouds over the site is known, due to the fact that clouds will provide an obstacle to the propagation of the fluorescence light from a cosmic ray shower.

2.6.8 Lidar System

The Pierre Auger Observatory utilizes four elastic lidars, one at each of the FD buildings [3]. Lidar stands for light detection and ranging. A lidar is composed of two main components, a laser which shoots a short laser pulse into the atmosphere and a detector that receives the light from the laser pulse backscattering off the molecules in the atmosphere. Here the term elastic lidar refers to the fact that the light detected by the lidar is of the same wavelength as the source of the light. This means that elastic lidar systems operate by utilizing Raleigh and Mie scattering processes. The lidars at the observatory are used for detecting cloud coverage over the observatory and the aerosol attenuation of the atmosphere. The current lidar system will be described in detail in the next chapters, as an upgrade to this system is the main topic of this thesis.

Chapter 3
The Lidar System

As mentioned in the previous chapter, one of the components of the Pierre Auger Observatory's atmospheric monitoring system is four lidar systems. The lidars are used to monitor both the aerosol content of the atmosphere and the position and height of clouds above the observatory. The intensity of the fluorescence light detected by the FDs during a cosmic ray shower is weakened by scattering and absorption of aerosols [2]. Also clouds are strong scatterers of the fluorescence light from a cosmic ray shower [2]. Thus, this information about the aerosol content of the atmosphere and cloud coverage is essential for the calibration of the FDs.

The lidars currently in use are unable to accurately measure the composition of the atmosphere for a distance of 0 km to approximately 1 km from the detector. In order to improve the lidar system in this near field range plans were made to add an additional detector to the existing system. This additional detector will focus on the composition of the atmosphere in the near field range. The design and implementation of the prototype detector for the upgrade to the current lidar is the main topic of this thesis.

3.1 Lidar Theory

Lidar at its simplest can be thought of as radar using lasers. However, unlike radar, which is used to image large objects such as aircraft, lidar is used to image the location and concentrations of molecules and aerosols (dust, fog, clouds, etc) in the atmosphere. In a lidar system a brief pulse of laser light, on the order of nanoseconds, is transmitted into the atmosphere in the direction under consideration. The light is then scattered or absorbed by gas molecules and aerosol particles. The backscattered light is collected by an optical receiver and analyzed to determine the composition of the atmosphere at distance points. A diagram of this process is shown in Figure 3.1.

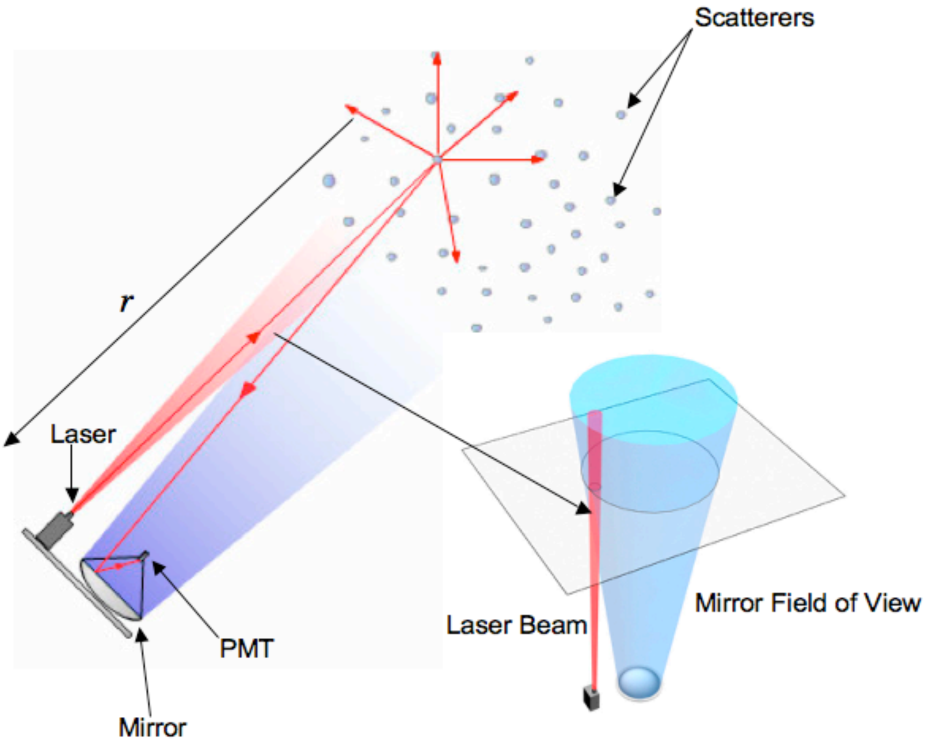

Figure 3.1: Diagram of a lidar system including the laser and optical receiver. [15]

The following is the lidar equation [1]

$$P(r) = G(r)\beta(r)\frac{C}{r^2}\exp\left(-2\int_0^r \alpha(z)\,dz\right) + P_{\mathrm{bg}}\,. \qquad (1)$$

This equation gives the power of the backscattered light received by the mirror collecting area at a given distance *r* from the detector (See Figure 3.1; [7]). The lidar equation has five main components. The first is the system factor *C*, which summarizes the performance of the detector [8]. It depends on the emitted laser power, the mirror collecting area, the laser pulse length and the system's detection efficiency. The system factor can be written as

$$C = P_0 \frac{c\tau}{2} A\eta\,, \qquad (2)$$

where P_0 is the average power of a single laser pulse. The term τ is the temporal pulse length and $c\tau$ gives the spatial length of the laser pulse. The term A is the area of the receiver optics. For the Pierre Auger Observatory's lidars this is the area of the mirrors. The term η is the system efficiency; which includes the optical efficiency of all the components in the lidar and the detection efficiency. The factor of 1/2 that appears in the system factor is due to the following. After the laser pulse is emitted at time t = 0, the backscattered light from the leading edge of the pulse is detected at time t. This means that the signal is from a distance $r_1 = \frac{ct}{2}$ away from the detector. At the same time backscattered light from the trailing edge of the laser pulse arrives at the detector from a distance $r_2 = \frac{c(t-\tau)}{2}$. So the length of the volume from which the backscattered light is received at a given time is $\Delta r = r_1 - r_2 = \frac{c\tau}{2}$ [8]. All of the components in the system factor are dependent on the lidar system's setup.

The second component in the lidar equation is associated with the range-dependent measurement of geometry, $\frac{G(r)}{r^2}$. Like the system factor, *C*, this geometric factor is dependent on the lidar setup. The r^{-2} term comes from the fact that the lidar detector area makes up a part of a spherical surface with radius *r*, which encloses the scattering volume, Figure 3.2. The term *r* is the distance from the scatterers in the atmosphere to the lidar receiver.

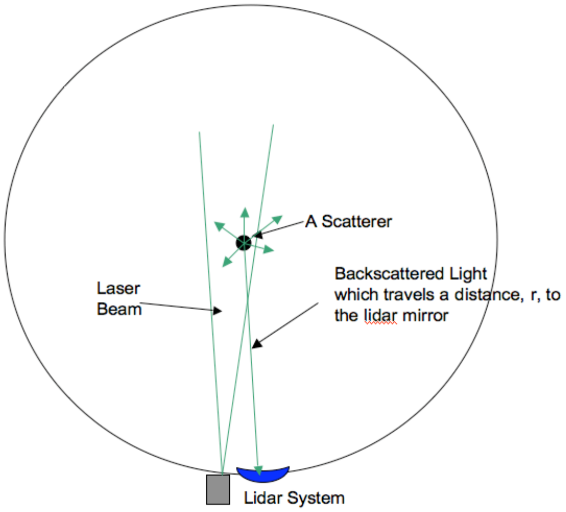

Figure 3.2: Diagram showing the particle at a distance *r* that backscatters the light detected by the lidar's mirror.

At distances close to the lidar detector little of the backscattered light is detected. This varies with distance from the lidar and depends on several factors including the laser beam diameter and divergence, the receiver field of view and imaging properties and the location of the laser beam axis and receiver axis relative to each other [8]. The term $G(r)$ is the laser beam receiver field of view overlap function. This function is the result of all geometric effects in the lidar system mentioned above.

An overlap function of 1 corresponds to the laser beam being completely within the field of view of the lidar detector, whereas an overlap of 0 would correspond to none of the laser being within the field of view of the lidar. An example of a good overlap and a poor overlap function are shown in Figure 3.3.

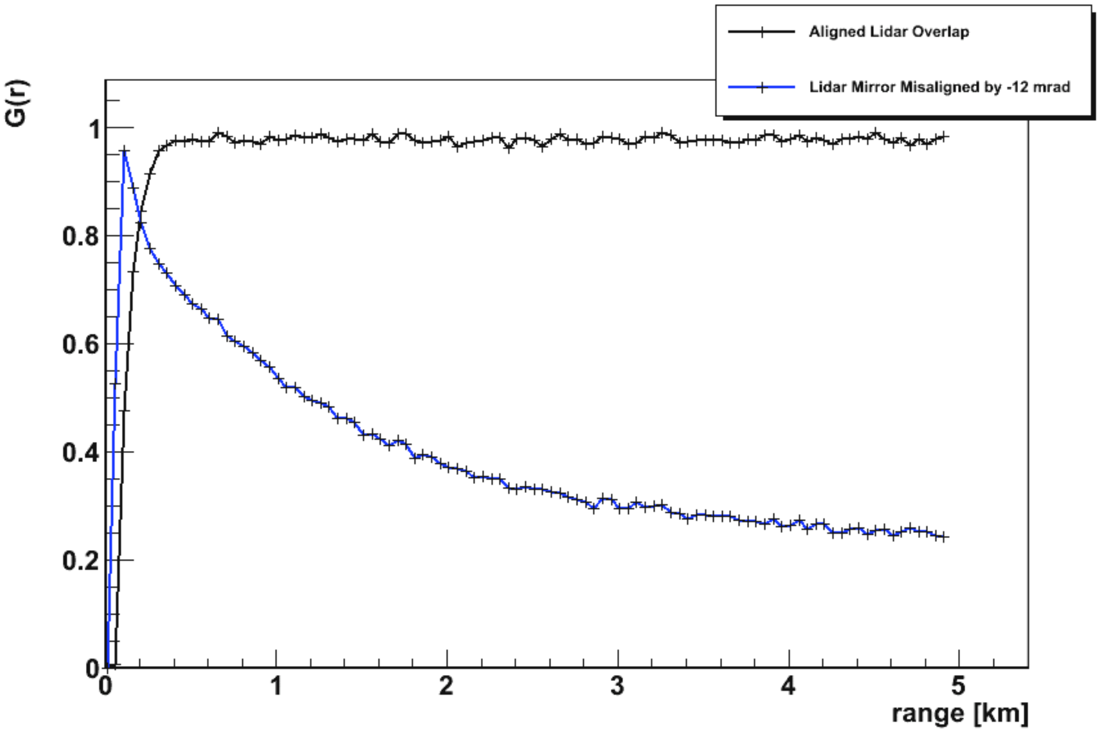

Figure 3.3: Example of an overlap function from an aligned lidar system and a poor overlap caused by a misalignment of the same system.

In Figure 3.3 the black line corresponds to an overlap for the lidar system currently in use at the Pierre Auger Observatory. This line shows a decent overlap over most of the range, the exception being the near field where the overlap fails to reach the maximum constant value. Once the overlap plateaus the laser beam is completely within the field of view of the lidar system's mirror. Figure 3.4 shows an aligned lidar system that would produce such an overlap.

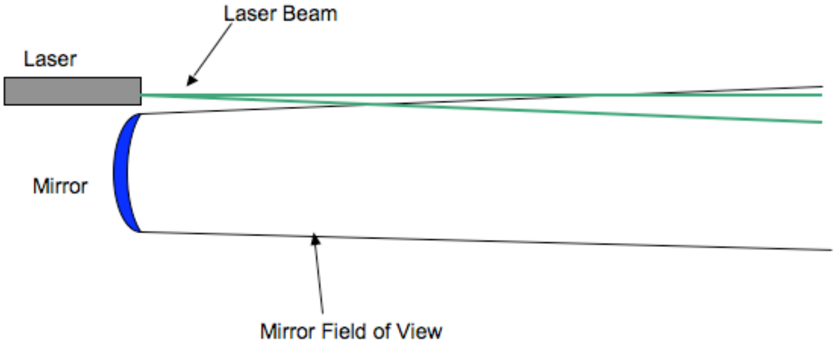

Figure 3.4: Diagram depicting an aligned lidar system that would produce the aligned overlap shown in Figure 3.3.

The blue line in Figure 3.3 corresponds to a poor overlap, which is produced by tilting the mirror in the lidar detector towards the laser beam by 12 milliradians. The field of view of the mirror converges with the laser beam quickly in the near field peaking at a range of less than 0.25 km. After this peak the laser and the field of view of the mirror diverge causing a decrease in the overlap function. The fact that the overlap function is not constant throughout the entire range makes this a poor overlap function. The lidar system misalignment that would produce such an overlap is shown in Figure 3.5.

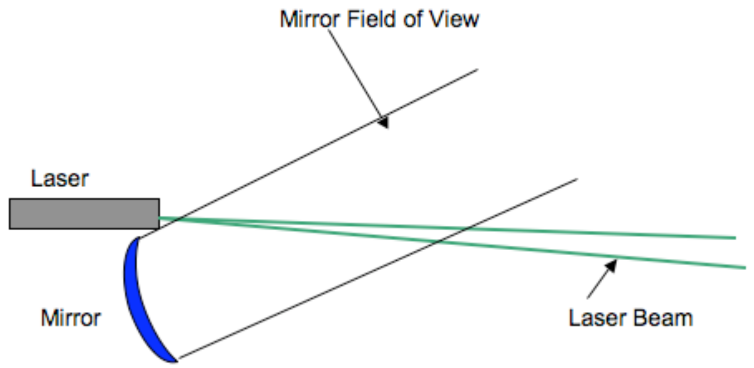

Figure 3.5: Diagram depicting a misaligned lidar system that would produce the poor overlap shown in Figure 3.3. Note that the misalignment is greatly exaggerated.

Ideally, the overlap geometry function would be 1 throughout the entire range but this is never the case; all lidar systems suffer from an incomplete overlap to some extent. The reason for this is the two different causes of an incomplete overlap. The first is when the laser beam is not within the field of view of the lidar detector; this case is shown in Figure 3.6. This source of incomplete overlap can be minimized by careful choice in the optical components of the lidar detector and their placement. The second cause is due to lidar detector components, such as the photomultiplier tube, blocking a portion of the signal. The second source of incomplete overlap can also be minimized by careful design of the photomultiplier tube holder. However, this effect can never be completely eliminated.

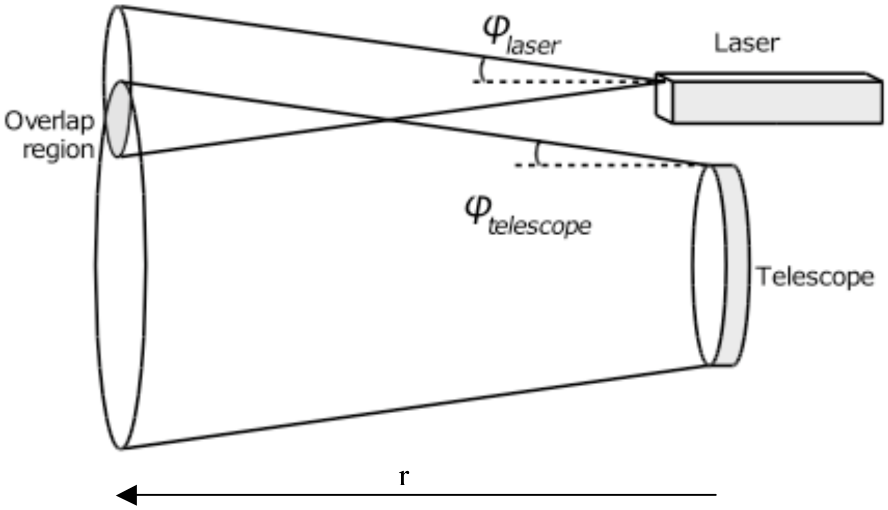

Figure 3.6: Schematic of an overlap for a lidar detector.

It is theoretically possible to determine the overlap function for any lidar system. However, this is not normally done. Due to the fact that the overlap function is dependent on the alignment of the lidar detector with the laser beam axis, theoretical calculation is difficult for mobile lidar systems, which can be become misaligned by mechanical vibrations over the course of normal operations. Small misalignments of the system can in some cases cause large changes in the overlap function. For the Pierre Auger lidar system the overlap $G(r)$ is determined experimentally [1].

The third component in the lidar equation is $\beta(r)$. This component is the range dependent backscattering coefficient [8]. This coefficient describes how much light is backscattered towards the lidar's mirror. It is the primary atmospheric parameter that determines the strength of the lidar signal. The factor $\beta(r)$ is composed of the sum of two components:

$$\beta(r) = \beta_{molecular}(r) + \beta_{aerosol}(r).$$

The term $\beta_{molecular}(r)$ is the molecular scattering coefficient. Molecular scattering comprises primarily scattering from nitrogen and oxygen molecules [8]. Being dependent on the density of the air, it decreases with increasing altitude. The second term $\beta_{aerosol}(r)$ is the aerosol scattering coefficient. Aerosol scattering occurs off a large variety of scatterers including dust, pollen and clouds [8]. This variety of scatterers means that the aerosol scattering coefficient varies over distance and time.

The fourth factor in the lidar equation is transmission term $\exp\left(-2\int_0^r \alpha(z)dz\right)$. This term takes into account the fraction of light that is lost on the way from the lidar to the scattering volume and back to the lidar's receiver [8]. It can have values from 0 to 1. The factor of 2 seen in the term is a result of the two-way transmission path. Extinction occurs from both scattering and absorption of light by molecules and aerosols. The sum of all extinction components is known as the extinction coefficient, $\alpha(r)$.

The fifth and final component of the lidar equation is P_{bg}, which is the background power. This background has two main sources. The first is starlight and other external light sources. The second is noise in the detector. For the Pierre Auger's lidar system the background is estimated by assuming that the power from the last 20% of the range, roughly 10 km, is solely due to background sources. The power is averaged in this region and used as P_{bg} in all calculations.

In order to obtain a simpler form of the lidar equation several steps can be taken [1]. First the background signal P_{bg} is estimated and subtracted giving the following $P'(r) = P(r) - P_{\mathrm{bg}}$. Next the quadratic decrease in the signal due to the solid angle is removed by multiplying by r^2. This gives the equation $Z(r)=r^2P'(r)$. Finally the signal must be calibrated at some fixed range r_c, resulting in the following $Z^*(r)=Z(r)/Z(r_c)$. The calibration point, r_c, is arbitrarily chosen in a region where the power of the system is stable. For the Auger's lidar system this region is usually in between 20 to 30 km. Once all of these steps have been performed the lidar equation takes the form:

$$S(r)=\ln Z^*(r)=\ln\frac{\beta(r)G(r)}{\beta(r_c)G(r_c)}-2\int_{r_c}^{r}\alpha(z)dz\,. \qquad (3)$$

This equation is known as the $S(r)$ function. For this thesis an even more simplified form of the lidar equation can be considered. For horizontal shots of the Pierre Auger Observatory's lidar system it is assumed that the atmosphere is homogeneous along the laser beam's path. Such horizontal shots are used as calibration shots for the observatory's lidars. These horizontal shots are used to experimentally determine the overlap function using the following method. For a homogeneous atmosphere the scattering coefficient $\beta(r)$ and the extinction coefficient, $\alpha(r)$ are independent of distance from the lidar [1]. Thus both $\beta(r)$ and $\alpha(r)$ become constants. In this case the first term in the $S(r)$ function becomes two terms a constant and $\ln G(r)$. The second term becomes $-2\int_0^r \alpha\, dz=-2\alpha r$. Thus $S(r)$ function takes the form:

$$S_{\exp}(r)=\ln G(r)-2\alpha r+\text{ constant}\,. \qquad (4)$$

The left side of Eq. 4 is obtained experimentally from a horizontal lidar signal. This is the form of the lidar equation that will be used in the sections on the considered upgrades to the Pierre Auger Observatory's current lidar system. To calculate the overlap function from Eq. 4 the function $S_{\exp}(r)$ is first plotted. Then α and the constant are found by performing a linear regression in a region where $G(r) \simeq 1$. In the plotted $S_{\exp}(r)$ function $G(r) \simeq 1$ occurs in regions where $S_{\exp}(r)$ is linear. Once α and the constant are found they are subtracted from $S_{\exp}(r)$. Giving the following:

$$\ln G(r) = S_{\exp}(r) + 2\alpha r - \text{ constant} . \tag{5}$$

Now to obtain $G(r)$, Eq. 5 just needs to be exponentiated, which gives the following equation,

$$G(r) = e^{S_{\exp}(r) - 2\alpha r + \text{constant}} . \tag{6}$$

Once $G(r)$ is found using this method it is utilized in removing the overlap function from all non-horizontal shots.

For non-horizontal shots the same procedure is performed to turn the lidar equation, Eq. 1, into the $S(r)$ function; except now the overlap is divided out before the calibration at the fixed range, r_c, is done. This means that the $S(r)$ function for non-horizontal shots of the lidar takes the form:

$$S(r) = 2\alpha r + \text{ constant} . \tag{6}$$

This is the final version of the $S(r)$ function, which is used to determine the atmospheric conditions. Also this is the form $S(r)$ takes if the overlap function, $G(r)$, is 1 throughout the entire range.

3.2 Introduction to the Current Lidar System

The Pierre Auger Observatory currently operates four lidar stations; one located at each of the fluorescence detector sites. The following sections are intended to briefly overview the current lidar system's hardware.

Each lidar station has three parabolic mirrors and a laser, Figure 3.7. The mirrors and laser are mounted to a steerable carriage giving the lidar a free range of pointing direction over the whole sky [17]. The mirrors in the lidar system are transversely offset from the laser axis. This setup has a major weakness in that the field of view of each of the mirrors does not contain the whole laser beam for a large portion of the near field. This weakness, Figure 3.6, leads to an incomplete overlap between the laser and mirrors in the near field [1]. The mirrors have a radius of 40 cm with a focal length of 41 cm [2]. Two of the three mirrors, Mirrors 0 and 2, have a transverse offset from the laser beam position of ~120 cm. These mirrors are located to the side and above the laser box respectively. The third, Mirror 1, has a transverse offset of ~170 cm, and is diagonally offset from the laser box [1]. The specifications for the existing lidar mirrors are summarized in the appendix and a diagram of the lidar system's setup is shown in Figure 3.7.

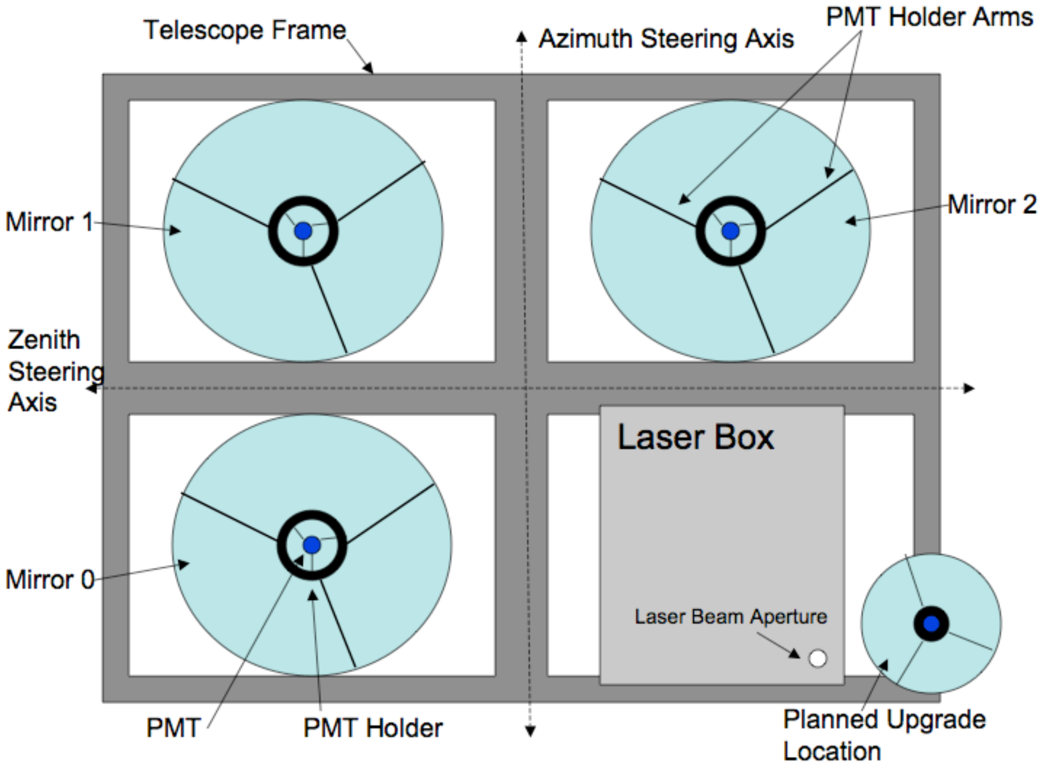

Figure 3.7: Layout of the lidar mirrors, photomultiplier tubes and laser box on the lidar frame, viewed head-on. Note this diagram is not to scale.

Each of the lidar stations uses a 333 Hz diode-pumped low-power DC30-351 Nd: YLF laser. The laser is mounted in a stiff box on an optical bench and the laser beam exits the box through an aperture in the front. The laser beam does not exit the aperture directly from the laser head. Instead it is redirected by several folding mirrors, which also remove contaminant wavelengths caused by lower harmonics [1]. The wavelength of the laser beam when it exits the aperture is purely 355nm.

Each mirror in the system is equipped with a single Hamamatsu R7400U miniature photomultiplier tube (PMT). These PMTs collect the backscattered light from the laser beam off the atmosphere.

3.2.1 Current Lidar System Simulation

The lidar system currently in use at the Pierre Auger Observatory has a poor overlap below a range of approximately 1 km. However, the simulation program used to model the lidar system is not completely accurate and gives a better overlap than the actual system. In this simulation the lidar system has a poor overlap below a range of approximately 0.4 km. This poor overlap is caused by the mirror optics currently in use and their configuration. The large transverse offset, the distance between the mirror axis and the laser beam, is the primary factor that contributes to the poor overlap. Because of the poor overlap, the data gathered in the near field is unreliable. It is important to have accurate data in this range due to the fact that most of the variation in the aerosol content of the atmosphere occurs in the near field.

Using a ray tracing simulation program written by Pierre Auger Collaboration member Matej Horvat, a post-doc at Nova Gorica Polytechnic in Slovenia, the overlap and *S(r)* functions are calculated. This simulation program models the current lidar system including the mirror, photomultiplier tube and the photomultiplier tube holder. The simulation models the path of the lidar's laser beam and randomly backscatters a set number of rays toward the lidar detector at set points along the range. The rays' paths are then tracked through the lidar detector's geometry. In the simulation valid rays are those that reflect off the mirror and strike the PMT's photocathode. The number of valid rays from a given range then determines the lidar power at that range. In the ray-tracing program, backscattered rays that strike any portion of the PMT holder are assumed to be absorbed and do not contribute to the lidar signal. From lidar power the S(r) function and the overlap $G(r)$ are calculated using the method discussed in Section 3.1.

In the original simulation, a cylinder with an outer radius of 6 cm was used to model the PMT holder. The PMT modeled in the simulation has a radius of 12.7 mm and a height of 61 mm, with a cathode window of radius 4.751 mm. For all other factors, such as mirror configuration and distance from the laser beam axis, the setup modeled in this ray-tracing program is that of Mirror 0 in the current lidar setup. A model of this lidar detector produced by the simulation is shown below in Figure 3.8.

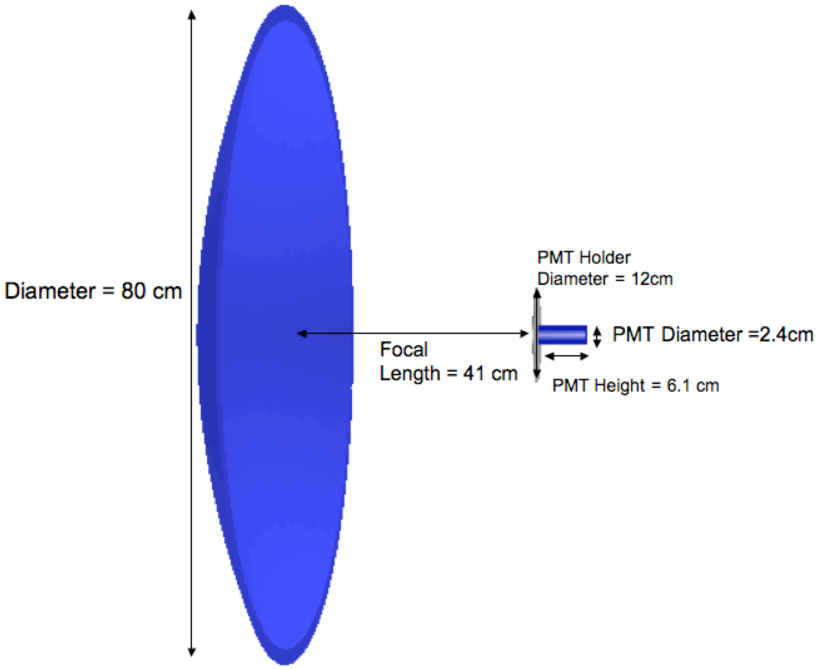

Figure 3.8: Model of a single mirror and PMT holder currently in use.

Using this ray-tracing program, an estimate of the overlap and S(r) functions for the current lidar system were obtained, Figure 3.9.

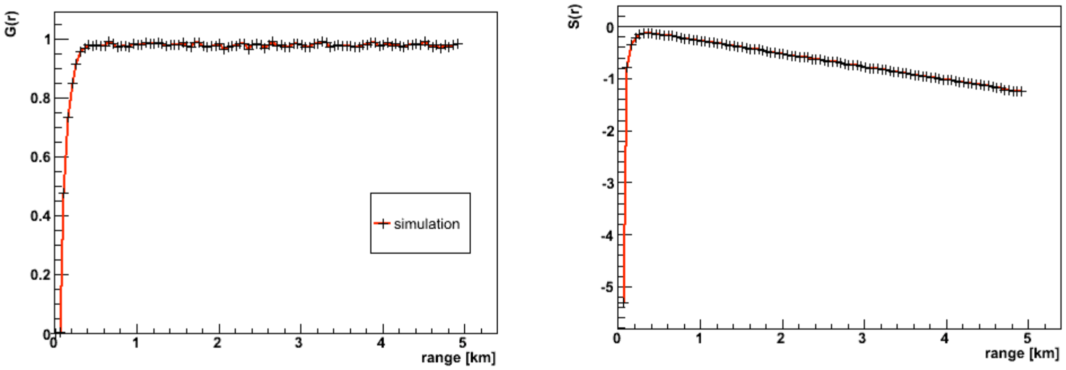

Figure 3.9: Overlap and S(r) functions obtained using a ray-tracing program with the setup shown in Figure 3.8.

For these two graphs it is apparent that the current system is blind below ~0.4 km. If the current setup were not blind below ~0.4 km, one would expect that the S(*r*) function would be a linear function throughout the entire range. This is not the case, as seen in the S(*r*) graph in regions below ~0.5 km. As discussed in section 3.1 the S(*r*) function takes on the simple linear form

$$S(r) = -2\alpha r + \text{constant}$$

for horizontal shots where α is a constant atmosphere volume total scattering coefficient and *r* is the distance from the detector to the scatterer, so long as the overlap function, $G(r)$, is 1 throughout the entire range [2]. This linear relationship is valid only for cases where the system has a complete overlap.

In this near field region below ~0.4 km, the incomplete overlap is a result of the laser beam not being completely in the field of view of the detector. Throughout the rest of the range, 0.5 km to 5 km, the laser beam is completely within the field of view of the mirror. However, the overlap still fails to reach a value of 1. The difference between the overlap found and the expected value of 1 is approximately 0.025. In the region between 0.5 and 5 km the overlap fails to reach 1 because the PMT and PMT holder block a portion of the backscattered rays. The effect of the PMT and PMT holder blocking the mirror can be seen in Figure 3.10. In order to determine the effect of the PMT and PMT holder blocking a portion of the backscattered rays the following steps were taken. First a series of overlaps with increasing PMT holder radii were found using the simulation program. For these overlaps all other variables, such as the mirror radius, are held constant and identical to those in Figure 3.8. For each of the overlap graphs the average overlap value was calculated in ranges where there was complete overlap, meaning that only overlap values beyond the range of ~0.4 km were used. After the average overlap value was found the change in the overlap, $\Delta G(r)$, was calculated. This $\Delta G(r)$ is equal to the difference between the theoretical ideal overlap, 1 and the average overlap calculated from the overlap graphs.

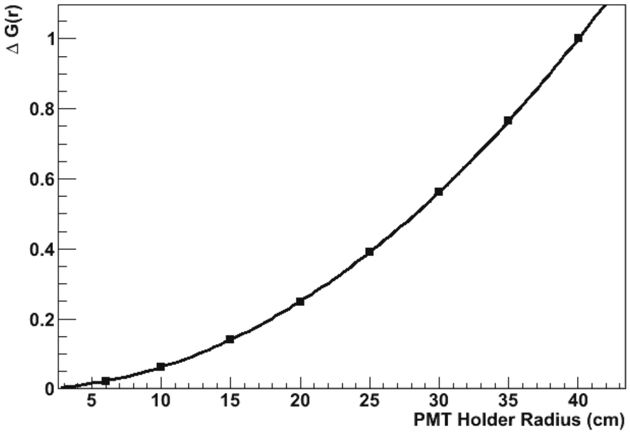

Figure 3.10: Graph showing the effect of the PMT holder and PMT blocking a portion of the backscattered rays on $G(r)$.

From the graph in Figure 3.10 it is clear that $\Delta G(r)$ is dependent on a constant times r^2, where r is the radius of the PMT holder. A fit of the line in Figure 3.10 reveals that $\Delta G(r) = \left(6.25 \times 10^{-4}\right) r^2$. This is identical to the ratio between the PMT holder radius and the radius of the mirror, meaning that the incomplete overlap in the range between 0.5 and 5 km is indeed due to the PMT holder blocking a portion of the backscattered light. This tells us that the simulation is accurately modeling the lidar system.

3.3 Considered Designs For The Upgrade To The Lidar System

The goal of this upgrade is to improve the lidar system in the near field by adding an additional lidar receiver to each of the four lidar systems. This additional lidar receiver will be optimized for data taking in near field.

Several designs for the upgrade to the lidar system were considered before construction of the prototype, which will be discussed in the following sections. Starting from the original lidar simulation program I created a total of five new simulations, one for each of the considered prototype designs. In each of the new simulations, code was added to account for the presence of PMT holder arms in addition to changes in the holder itself, as well as changes in the mirror size and focal length. Once the changes in the optics and PMT holders were made, each of the programs were used to determine the S(*r*) functions and overlap functions of each of the new designs.

Once the S(*r*) functions and overlap functions were found for perfect alignment, a series of simulations were run with misalignments present, such as the PMT being off the focal point of the mirror. These simulations give a rough estimate of the misalignment tolerance of the prototype designs. In the following sections the various designs are considered.

3.3.1 First Design

The first design for the near-field receiver is composed of a single 7.5 cm radius parabolic mirror with a focal length of 30 cm. Three arms connect the mirror to a PMT holder with a radius of 3 cm. The configuration for this design is shown below in Figure 3.11.

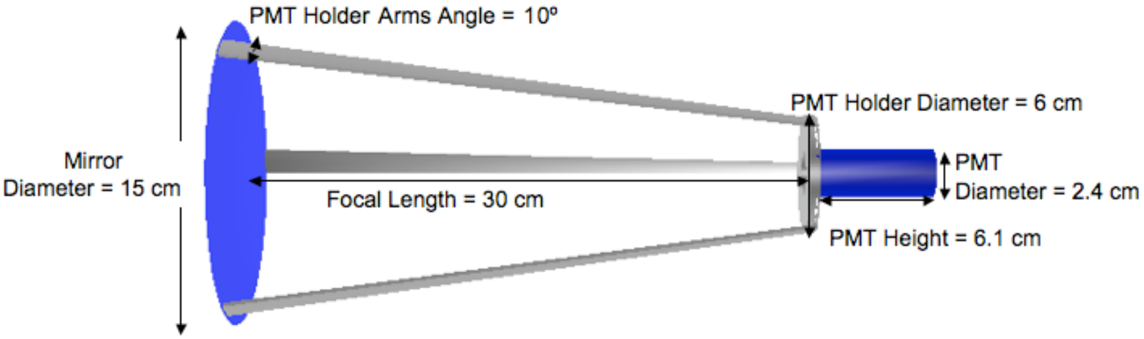

Figure 3.11: First possible design for the near-field receiver.

This receiver would be mounted to the telescope frame next to the laser enclosure opposite Mirror 0 in the current setup. The minimum transverse offset, which is the distance between the laser beam and the mirror's axis, is ~18 cm. Using the ray-tracing program, the overlap and S(*r*) functions were found, shown in Figure 3.12. For this design the S(*r*) function follows the expected linear trend. For the overlap function the only source of incomplete overlap is from the pmt holder blocking a portion of the backscattered rays. This is seen throughout the entire range, as the overlap value never reaches 1.

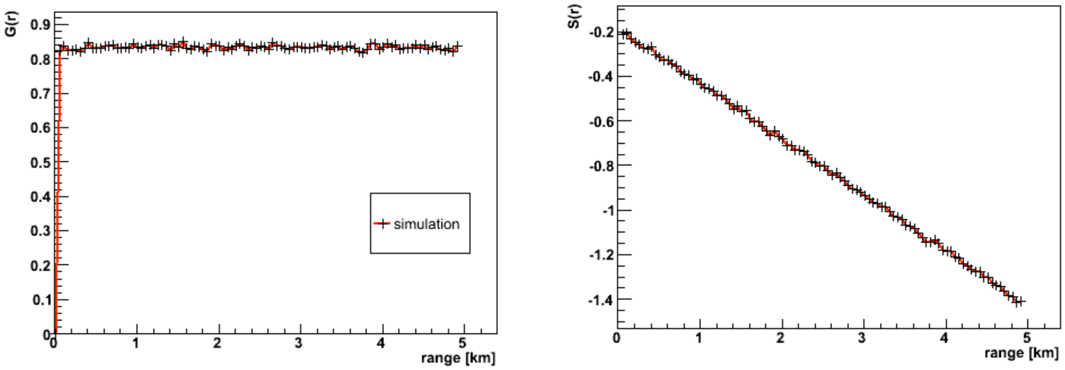

Figure 3.12: Overlap and S(r) functions obtained using the setup shown in Figure 3.11.

For comparison of the first design to the current lidar setup the overlaps for both are plotted below in Figure 3.13. For the first design the overlap levels off at a smaller value as compared to the original lidar system. This is due to the size of the mirror used in the first design. Because the mirror is much smaller the effect of the PMT holder and holder arms blocking a portion of the backscattered rays is much more apparent than in the original lidar system. In the original system the mirror is large enough that the effect of the PMT holder and arms is much smaller. Indeed, in the original simulation the PMT holder arms were not taken into account. The obvious improvement of this design is the fact that the overlap value reaches its maximum and levels off to a constant value sooner in the range, as compared to the original system. This is due to the smaller transverse offset for the first design. The original lidar system had a transverse offset of 120 cm; which is much larger compared to the ~18 cm offset for the first design.

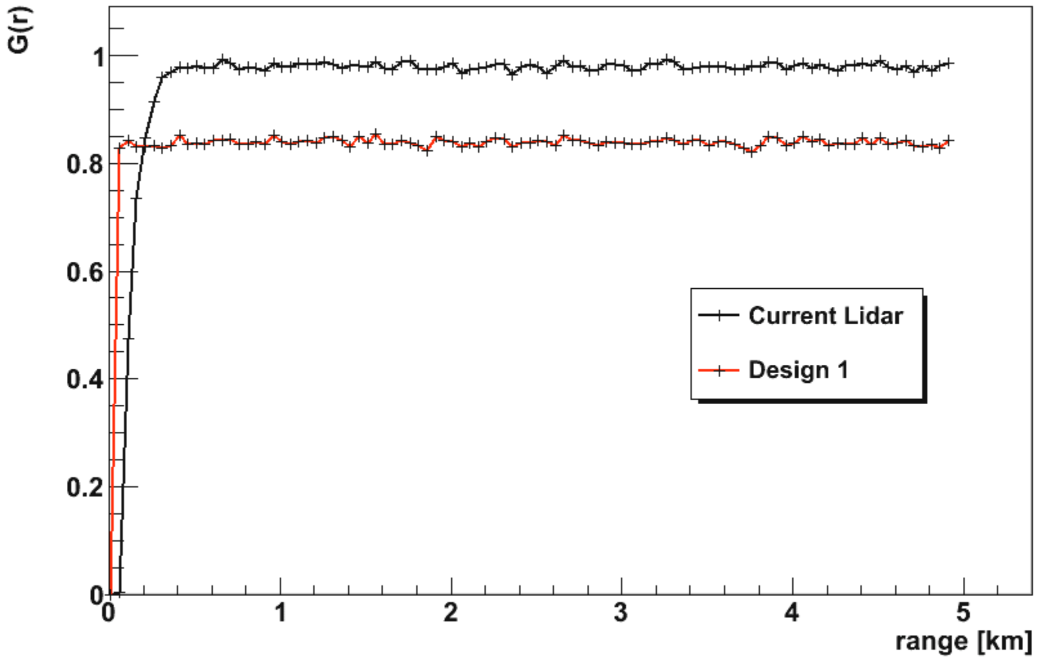

Figure 3.13: Comparison plot between the overlap of the first design and the existing lidar setup.

3.3.2 Second Design Version I

Similar to the first design, the second contains a 7.5 cm radius parabolic mirror with a focal length of 30 cm. Like the first design this design would also be mounted to the telescope frame next to the laser enclosure opposite Mirror 0, with a minimum transverse offset of ~18 cm. However, instead of three support arms to hold the PMT, the second design is similar to a telescope. This design was studied because concerns were raised about the stability of the alignment for the first design. It was believed that the three thin PMT holder arms in the first design would be susceptible to mechanical vibrations when the lidar mount was in motion. This would cause the system to become misaligned and such a misalignment could lead to a poor overlap.

For the second design, three possible versions were examined. The first contains a tube (a right cylinder) with an inner radius of 7.5 cm. The mirror is positioned at the far end of the tube. At the open end of the tube, three arms are modeled by using three segments of a disk, each subtending an azimuthal angle of 10 degrees. These arms connect to a 3 cm radius PMT holder. The setup is shown below in Figure 3.14.

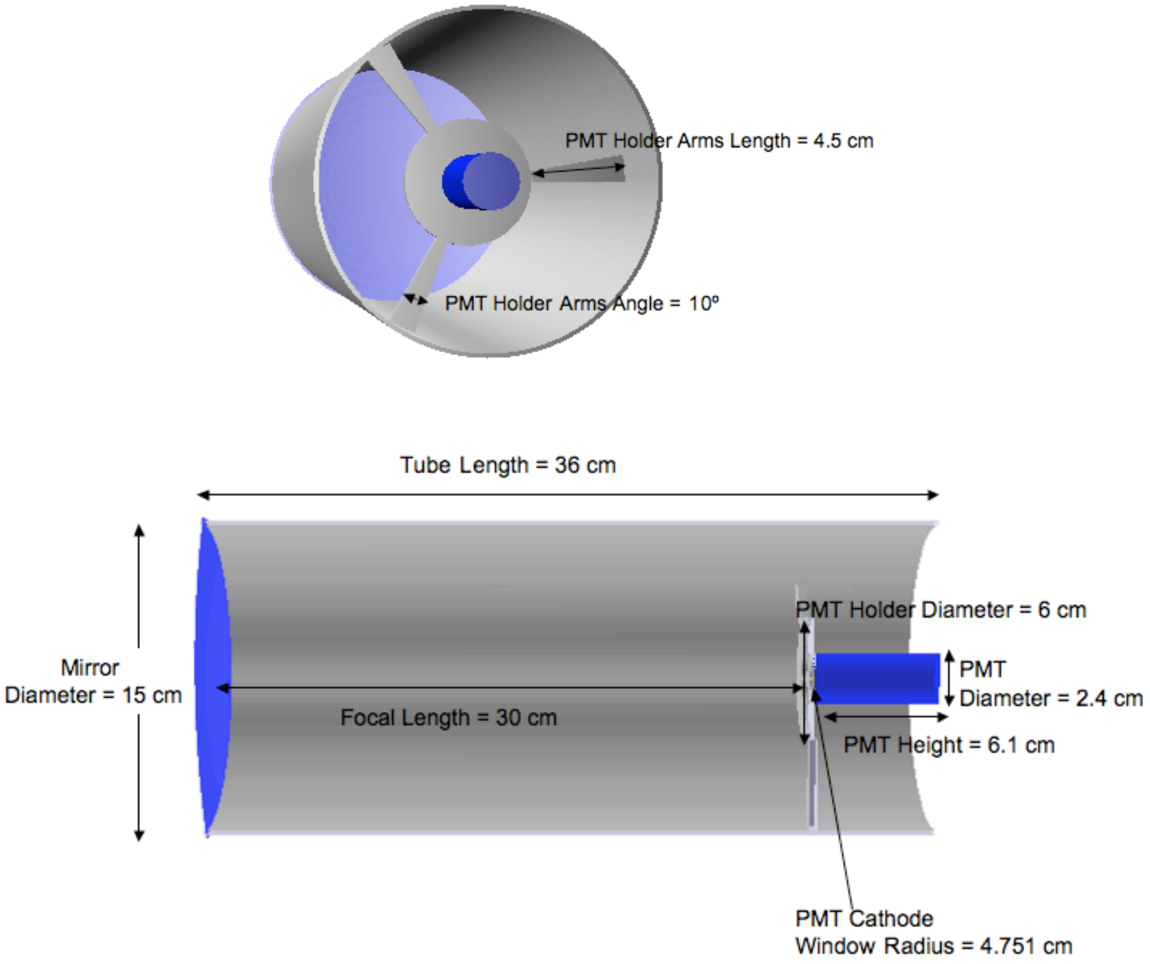

Figure 3.14: Top: Front view of the first version of the second design. Bottom: Side view of the first version of the second design.

As with the first design, the overlap and S(*r*) functions were estimated using a ray-tracing program, and the results are shown below in Figure 3.15. As with the first design the S(*r*) function for the first version of the second design shows the desired linear trend. The overlap function for this design, however, also suffers from the effect of a portion of the backscattered light being blocked by the PMT holder. For this design the effect of the backscattered light is worse as compared to the first design.

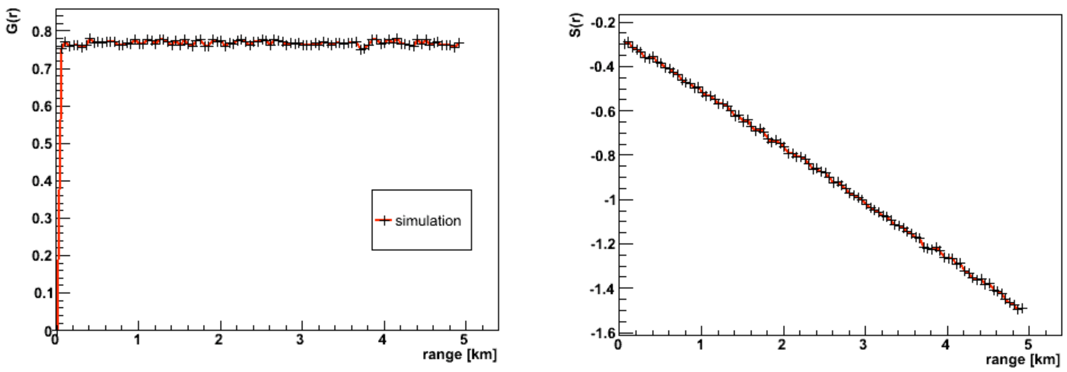

Figure 3.15: Overlap and S(r) functions for the first version of the second possible design shown in Figure 3.14.

For comparison the overlaps for the first design, first version of the second design and the current setup are shown below in Figure 3.16. Similar results are seen for the first version of the second design as were seen for the first design. The overlap reaches its maximum value and levels off sooner in the range as compared to the original lidar system. This is again due to the small transverse offset. However, maximum value for the overlap is lower than the first design. This is due to an increase in the size of the PMT holder arms, which block a portion of the backscattered rays.

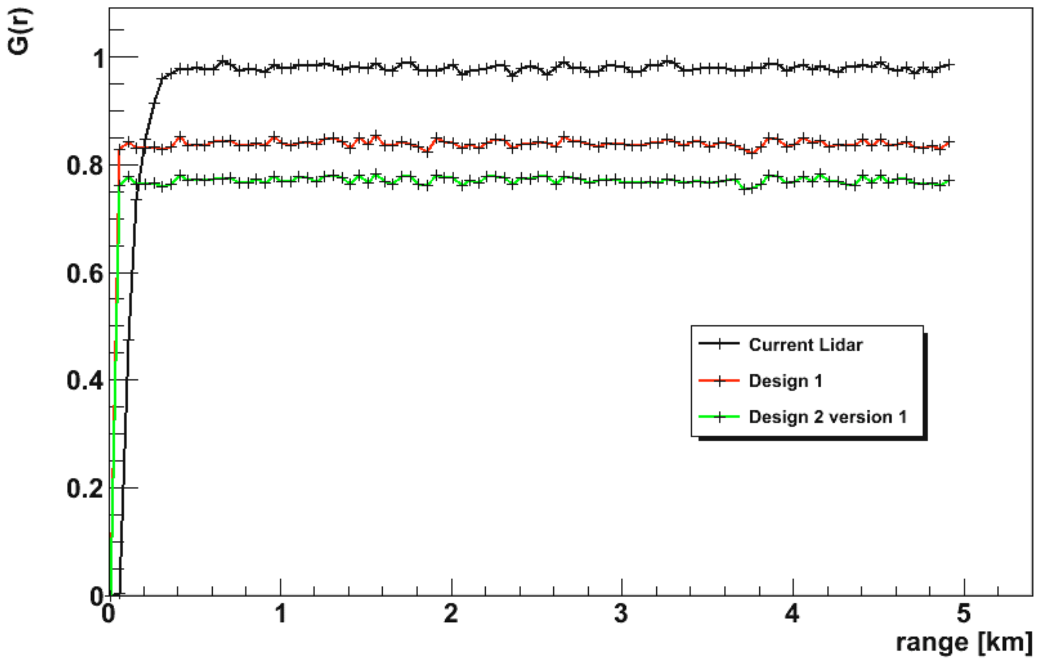

Figure 3.16: Comparison plot between the overlap of the first design, first version of the second design and the existing lidar setup.

3.3.3 Second Design Version II

The second version of this design also contains a tube (a right cylinder) with an inner radius of 7.5 cm. Again, at the open end; three arms connect to the 3 cm radius PMT holder. However, in this version the arms subtend an azimuthal angle of 5 degrees, making them thinner than the first version of this design. This version is shown in Figure 3.17.

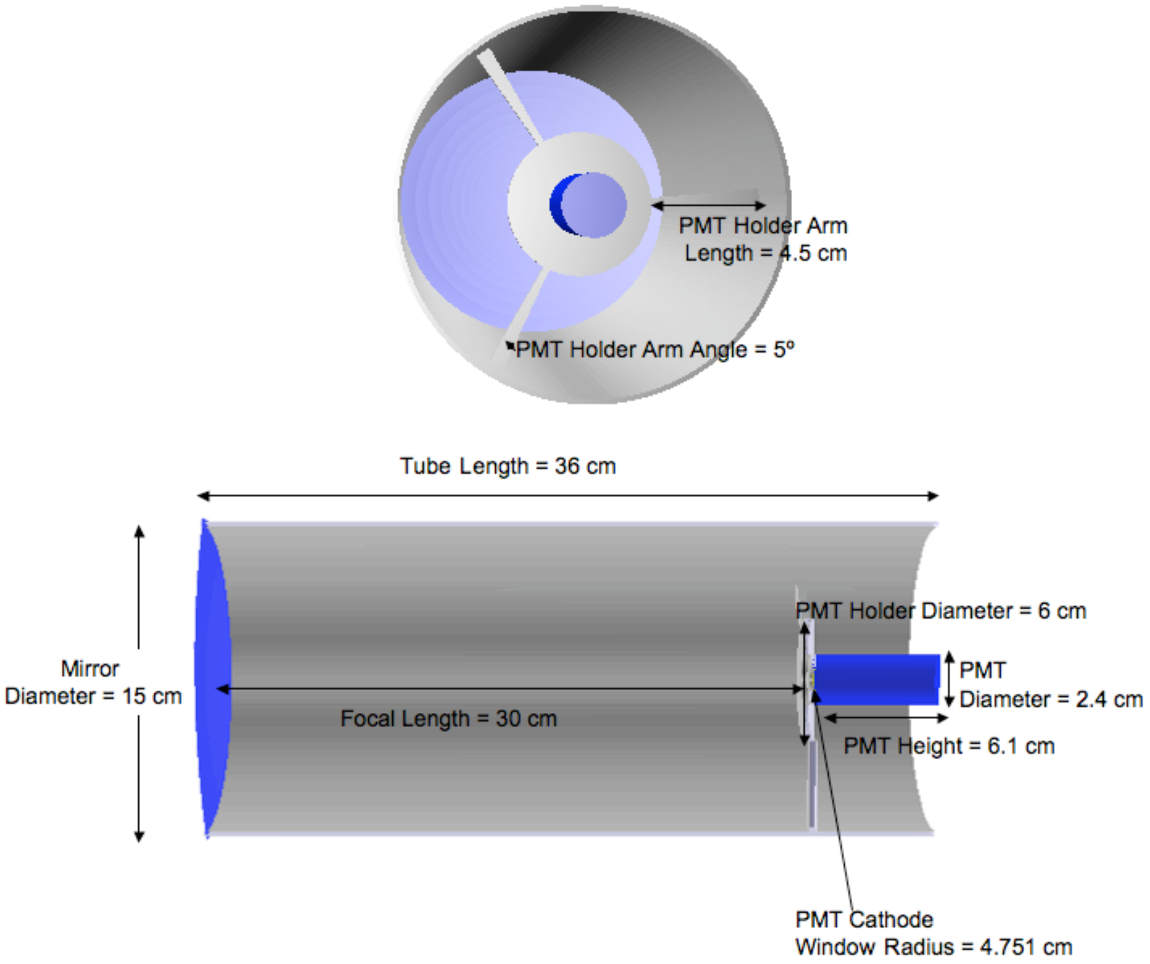

Figure 3.17: Top: Front view of the second version of the second design. Bottom: Side view of the second version of the second design.

Again, the overlap and S(*r*) functions were found using the ray-tracing program and are shown in Figure 3.18. As with the previous designs the S(*r*) function shows the desired linear trend. As for the overlap function there is an improvement as compared to the first version of the second design. However, it is still not as good an overlap function when compared to the first design.

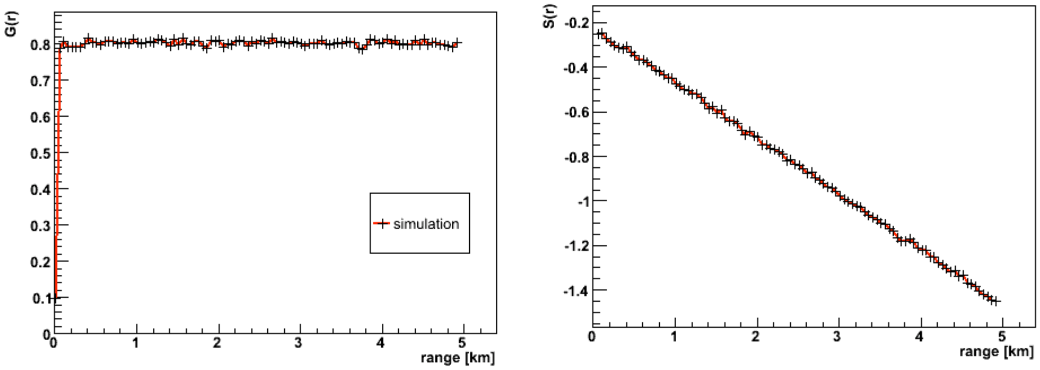

Figure 3.18: Overlap and S(r) function for the second version of the second design as shown in Figure 3.17.

In order to determine the effect of the PMT holder arm size on the overlap, a similar study to the one that produced Figure 3.10 was done. However, here instead of increasing the PMT holder size the angular width of the PMT holder arms was increased. From Figure 3.19 it is clear that increasing the size of the PMT holder arms will cause an increase in $\Delta G(r)$. This corresponds to a decrease in the overlap. So, clearly, the smaller the PMT holder arms are the better the overlap will be.

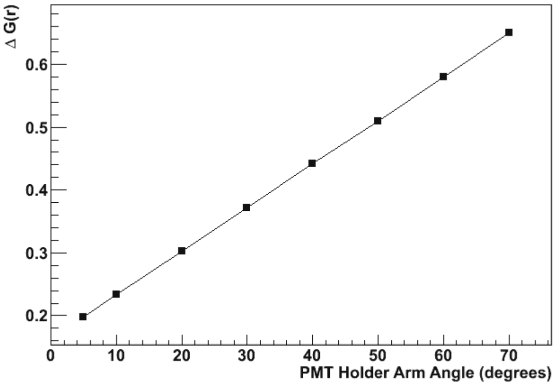

Figure 3.19: Comparison plot between the overlap of the second version of the second design and the existing lidar setup.

3.3.4 Second Design Version III

The final version of the second design uses a cone for the support of the PMT holder, with an inner radius of 7.5 cm at the end containing the mirror and an inner radius of 10 cm at the open end. At the open end of the tube, three arms are modeled by using three segments of a disk, each subtending an azmuthal angle of 10 degrees. These arms connect to a 3 cm radius PMT holder. The setup is shown below in Figure 3.20.

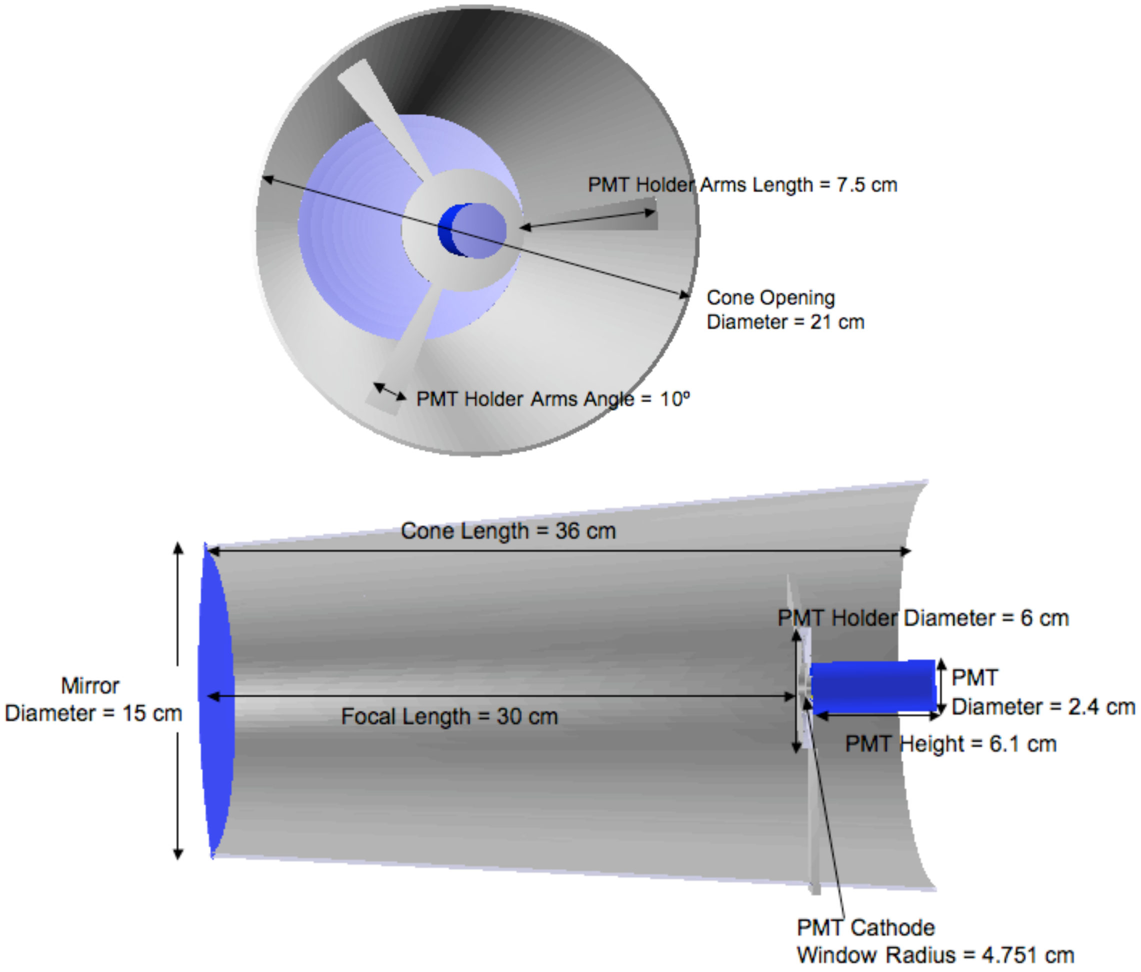

Figure 3.20: Top: Front view of the third version of the second design. Bottom: Side view of the third version of the second design.

As before, the overlap and S(*r*) functions were found using the ray-tracing program, shown in Figure 3.21. As with as the previous designs the S(*r*) function shows the expected linear trend. The overlap function, however, is almost identical to the overlap for the first version of the second design.

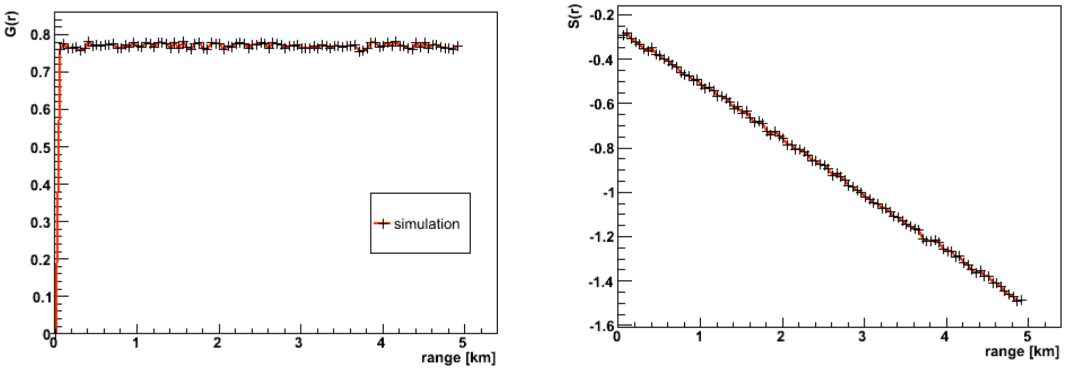

Figure 3.21: Overlap and S(r) function for the third version of the second design as shown in Figure 3.20.

For comparison the overlap graphs for the first design, the first version, the second version and third version of the second design and the current setup are shown in Figure 3.22. Again similar improvement is seen in how quickly the maximum value for the overlap is achieved due to the small transverse offset. However, the same drawback of the PMT holder and holder arms blocking a portion of the backscattered light is still present in the third version of the second design. It should be noted that the first version of the second design is practically identical to the third version of the second design making it difficult to see in Figure 3.22. This means that using a cone shape for the PMT holder arm support instead of a cone does not improve the overlap.

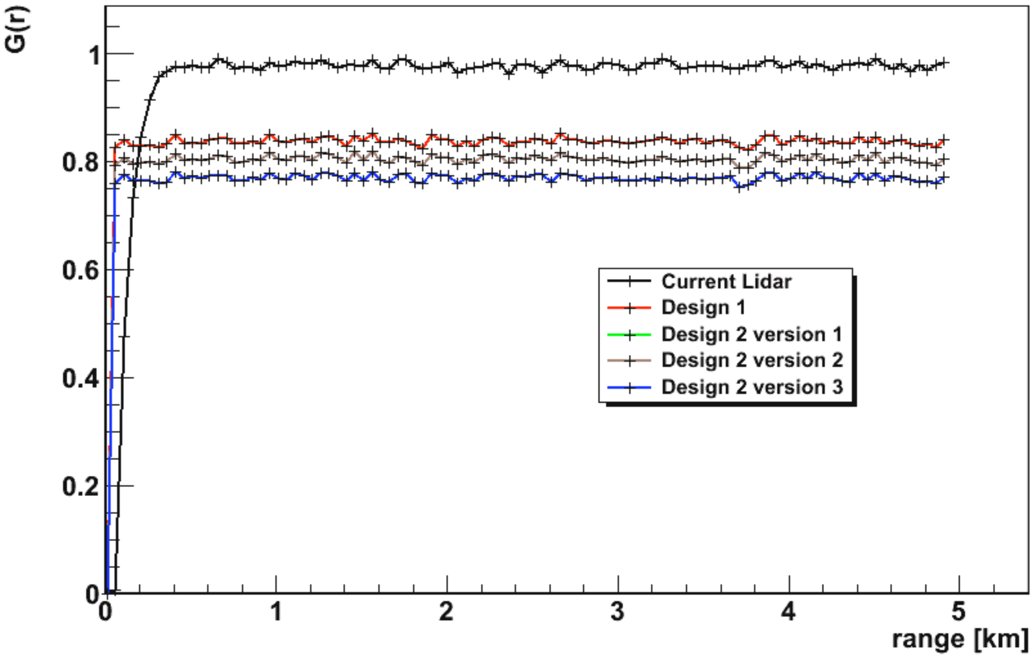

Figure 3.22: Comparison plot between the overlap of the third version of the second design and the existing lidar setup.

3.3.4 Third Design

The third design is similar to the second version of the second design, the main difference being the size of the mirror. In the third design the mirror has a radius of 17 cm, as opposed to the 7.5 cm of the previous designs. The PMT holder is composed of a tube (a right cylinder) with an inner radius of 17 cm and at the open end of the tube 3 arms attach to a 3 cm radius pmt holder. The arms subtend an azimuthal angle of 5 degrees similar to the second version of the second design.

As with the previous designs the S(r) function and the overlap were found using the ray-tracing program, shown below in Figure 3.23. Again the S(*r*) function shows the linear trend we are looking for. However, unlike the previous designs the maximum value for the overlap is much closer to 1. This means that the third design has the best overlap when compared to all the other designs.

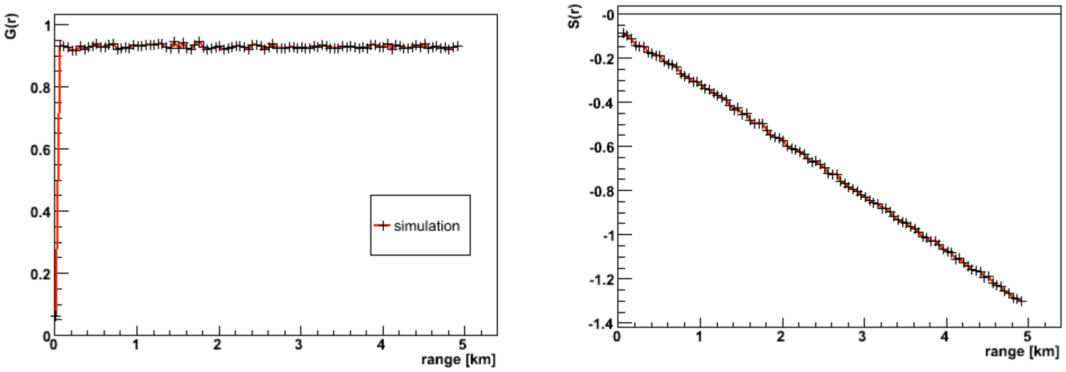

Figure 3.23: Overlap and S(r) function for the third design.

For comparison the overlap graphs for all the considered designs and the current setup are shown in Figure 3.24. Due to the larger size of the mirror in the third design the maximum value for the overlap is higher than the previous designs. The larger size of the mirror, as compared to the previous designs, reduces the effect of the PMT and PMT holder blocking a portion of the received rays. Also the transverse offset of the mirror to the laser beam axis is still small enough to insure that the maximum overlap value occurs at a closer range as compared to the current lidar system.

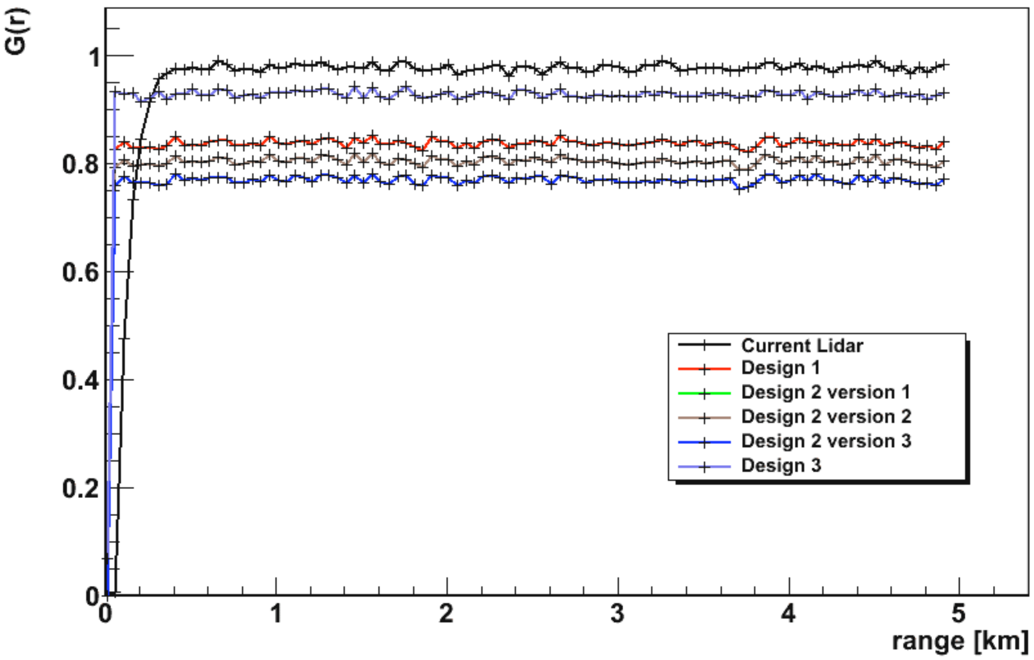

Figure 3.24: Comparison of $G(r)$ for all of the considered designs.

3.3.6 Transverse Offset Effect

An increasing transverse offset between the laser beam and the lidar detector mirror will lead to a poorer overlap in the near field. To demonstrate the relationship between the transverse offset and the overlap several simulations where run with increasing offset using the second version of the second design. A sample of the overlap functions produced by the simulation is shown in Figure 3.25.

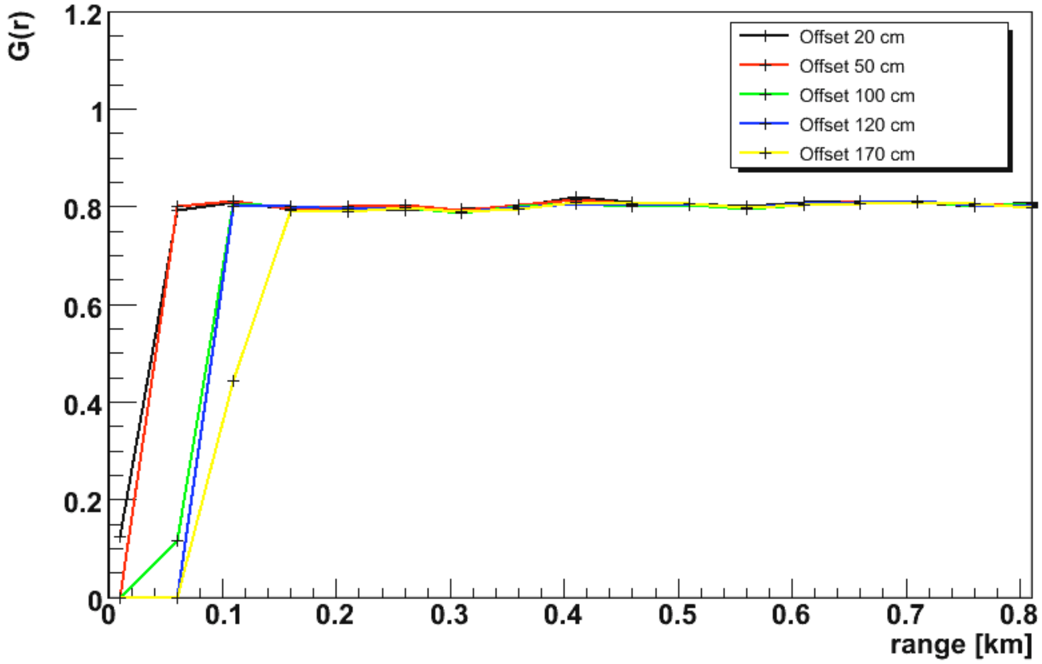

Figure 3.25: Overlap functions for the second version of the second design with increasing transverse offsets.

In Figure 3.25 it is clear that an increase in the transverse offset between the laser beam and the lidar mirror causes the overlap to reach its maximum value later in the range. This effect is seen for all of the designs.

A study was done to demonstrate that an increasing transverse offset causes the overlap to reach its maximum value later in the range and how this also depends on the mirror's radius. For this study a series of overlap plots were made for mirrors of varying radii and transverse offset. The lidar setup used in this case is similar to the original lidar in that the PMT holder arms were not included in the simulation. A PMT holder with a radius of 3 cm was used in all of these overlap plots. The PMT configuration was the same as the PMT in the original lidar and the mirror's focal length was set to 41 cm. The five different mirror radii used were 10, 20, 30, 40 and 50 cm. These mirrors were initially placed as close to the laser beam as possible and then moved outwards, increasing the transverse offset, Figure 3.26.

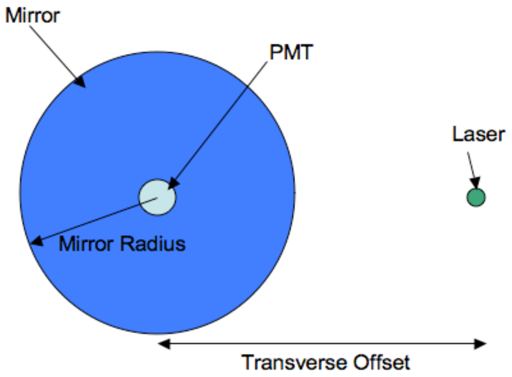

Figure 3.26: Diagram of the lidar system with the transverse offset as seen looking towards the mirror.

For each of the overlap plots taken two values were calculated; $\Delta G(r)$, which is the change in overlap from the ideal value of 1, and R(95%), which is the range when the overlap has reached 95% of its maximum value.

In Figure 3.27 the $\Delta G(r)$ value found for each mirror at each offset is plotted. The $\Delta G(r)$ value is mostly constant with increasing offset and increases with decreasing mirror radius. The increase in $\Delta G(r)$ is due to the smaller mirrors having more light blocked by the PMT holder. This also shows that the increasing transverse offset does not affect the maximum value the overlap will reach.

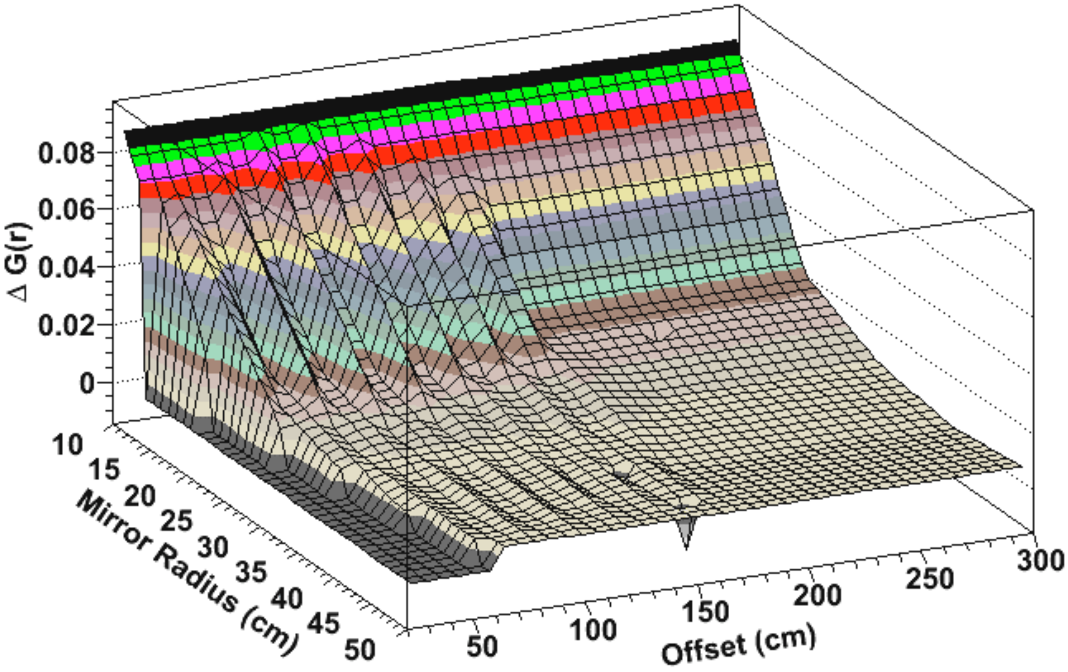

Figure 3.27: Plot of $\Delta G(r)$ for various mirror radii and transverse offset values.

In Figure 3.27 for offsets of less than 150 cm there does appear to be fluctuations in $\Delta G(r)$. This is not due to a real property of the lidar, but is rather a result of the graphing program used to produce the plot and the number of data points taken. Increasing the number of data points in this region will remove the fluctuations.

In Figure 3.28 the R (95%) value found for each mirror at each transverse offset is plotted. The R (95%) value increases with increasing mirror radius and increasing transverse offset. This increase in R (95%) means that the larger the mirror is and the further it is from the laser the greater the range will be before the laser beam is completely within the mirror's field of view.

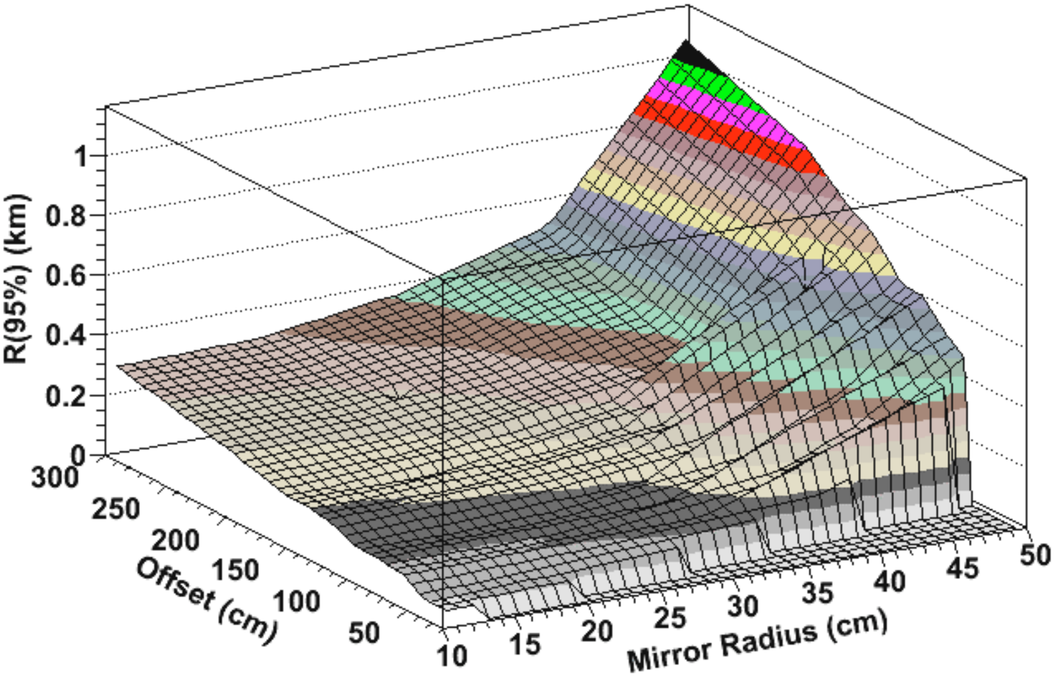

Figure 3.28: Plot of the range at which the overlap reaches 95% of its asymptotic value for various mirror radii and transverse offsets.

Figure 3.28 also appears to have fluctuations for offsets of less than 150 cm. This is the same as it was for Figure 3.27; these fluctuations are not the result of a property of the lidar and increasing the number of data points will remove them.

3.3.7 Design Misalignments

Four different misalignments were investigated for each of the considered designs in order to estimate the tolerance of each. The first misalignment is that of the PMT along the mirror axis. This misalignment corresponds to a defocusing of the lidar system by moving the PMT off of the mirror's focal point. In the ray tracing simulation this is achieved by moving the PMT along the z-axis. A diagram of this is shown in Figure 3.29.

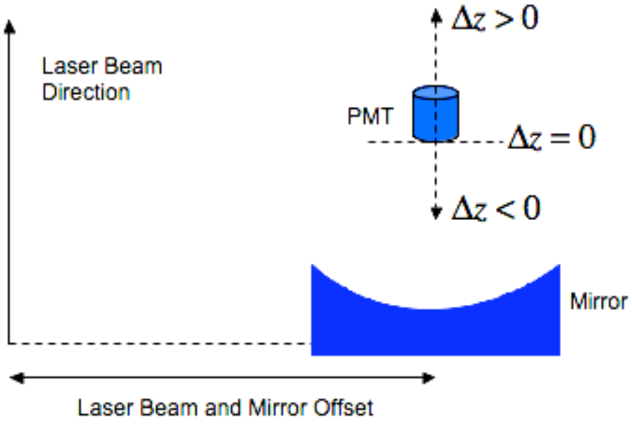

Figure 3.29: Diagram of the misalignment of the PMT along the mirror axis.

The second misalignment is that of the PMT lateral to the mirror axis. For this misalignment there are two directions to consider, movement of the PMT along the x-axis and along the y-axis. The x-axis misalignment is a movement towards and away from the laser beam, with negative values corresponding to a movement towards the laser. The y-axis misalignment corresponds to moving the PMT upwards and downwards while maintaining the same distance from the laser beam axis. A diagram of this misalignment is shown in Figure 3.30.

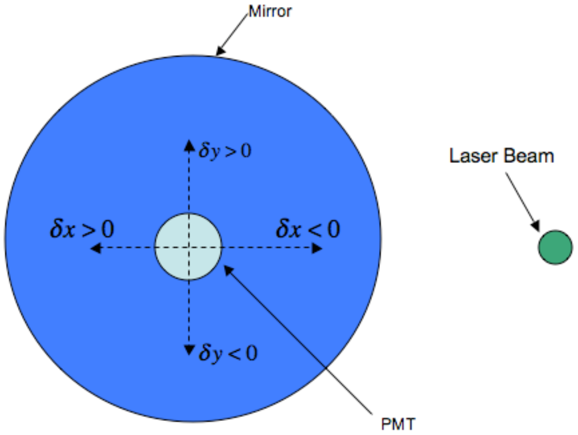

Figure 3.30: Diagram of the lateral misalignment of the PMT as seen looking towards the mirror.

The third misalignment is that of the mirror in theta. This corresponds to a tilt of the mirror towards and away from the laser beam axis, where a negative theta represents a tilt toward the laser and a positive away from the laser. This misalignment is shown in Figure 3.31.

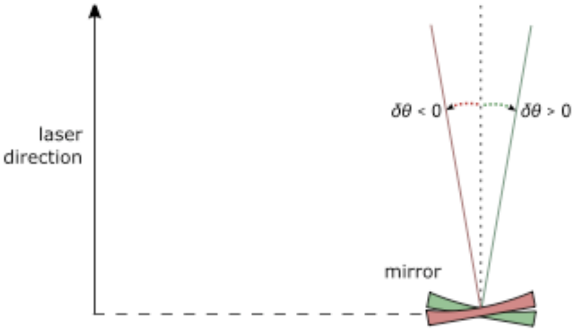

Figure 3.31: Diagram of the misalignment of the mirror in theta [16].

The fourth misalignment considered is that of the mirror in phi. This misalignment is a tilt of the mirror forward or backwards. This final misalignment is demonstrated in Figure 3.32.

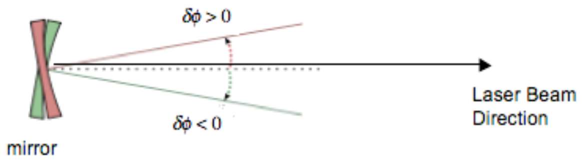

Figure 3.32: Diagram of the misalignment of the mirror in the phi direction. In this diagram the lidar system is viewed from the side. [16]

For each of the considered misalignments a series of overlap plots were made with the simulated design increasingly misaligned. For each of the plots with a misalignment the value of the overlap was recorded at four ranges; 0.2 km, 0.5 km, 1.0 km and 2.5 km. Once the overlap values from the misaligned graphs were found, a percent difference was calculated using the overlap value of an ideally aligned system as the reference value. For all misaligned graphs the percent difference was calculated using the following equation:

$$\frac{(\text{ideal overlap at 1 km})-(\text{overlap with misalignment at 1 km})}{(\text{ideal overlap at 1 km})}*100$$
$$= \text{percent difference between ideal and misaligned at 1 km}$$

This was done for each of the four ranges. For this study if the percent difference calculated for a misaligned lidar design is 5% or below the lidar is considered to be within tolerance. A percent difference greater than 5% from the ideal alignment is outside of the acceptable tolerance and is to be avoided.

It was found that all of the designs showed the same trends in tolerance of misalignments. For the first design and all versions of the second design the tolerance was practically identical for all of the misalignments studied. The third design consistently had a smaller tolerance for all of the misalignments.

	0.2 km	0.5 km	1.0 km	2.5 km
Design 1	-17.8 – 18.6	-18.4 – 19.1	-18.5 – 19.1	-18.6 – 19.1
Design 2 v1	-17.8 – 18.7	-18.4 – 19.0	-18.5 – 19.0	-18.7 – 19.0
Design 2 v2	-17.8 – 18.7	-18.4 – 19.0	-18.4 – 19.2	-18.6 – 19.1
Design 2 v3	-17.9 – 18.6	-18.4 – 19.0	-18.4 – 19.0	-18.5 – 19.0
Design 3	-5.7 – 8.1	-6.1 – 8.1	-6.2 – 8.1	-6.2 – 8.0

Figure 3.33: Design tolerances for the displacement the PMT along the z-axis in millimeters.

The table in Figure 3.33 gives the design tolerances for a misalignment of the PMT along the z-axis for each of the designs considered. For each design and each range considered the maximum and minimum allowed misalignment is given. Tables containing a summary of the results of the other studied misalignments for each design are located in the Appendix. These tables give the range of misalignment each design may have and still be within the 5% tolerance. This is done for each design and each of the four considered ranges.

The following graphs in this section are samples of the results from the misalignment studies conducted for each of the proposed designs. All of the shown graphs are from tolerance studies of the second version of the second design. For the case with a defocusing of the PMT by moving forwards or backwards along the z-axis the lidar remains within tolerance from approximately -18 mm to 19 mm. Between these values the overlap remains roughly constant with very little deviation from the ideal overlap. Once the misalignment is outside the acceptable tolerance the overlap value decreases sharply. The two graphs in Figure 3.34 are the percent difference graphs for this misalignment.

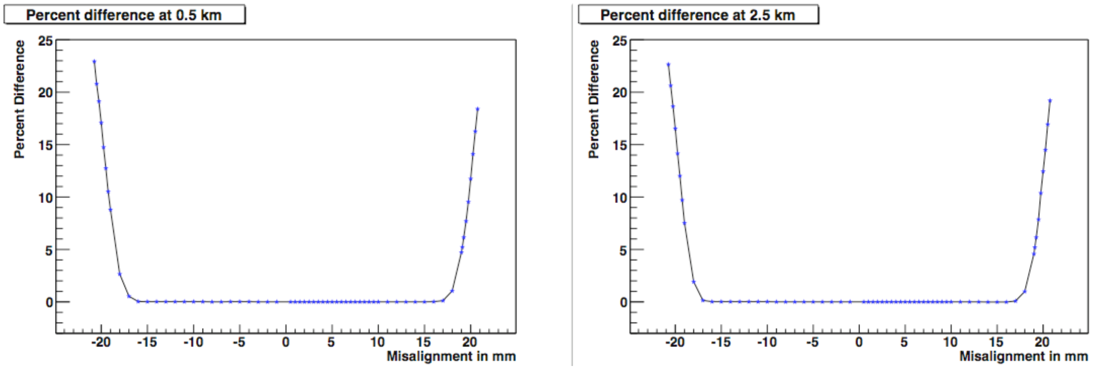

Figure 3.34: The left graph is the percent differences at 0.5 km for a series of misalignment plots with a defocusing of the PMT. The right graph is the percent differences at 2.5 km for a series of misalignment plots with a defocusing of the PMT.

There are two cases with a misalignment of the PMT lateral to the laser beam. For the case where the PMT was moved along the x-axis, towards or away from the laser beam, the tolerance was approximately -2.4 mm to 2.1 mm. For misalignments between these values the overlap remains roughly constant with very little deviation from the ideal overlap. Once the misalignment is outside the acceptable tolerance the overlap value decreases sharply. The two graphs in Figure 3.35 are the percent difference graphs for this misalignment.

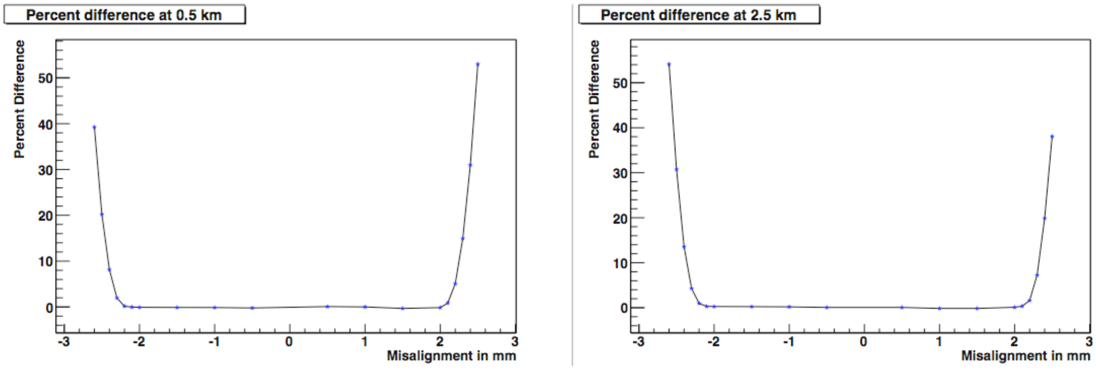

Percent difference at 0.5 km

Percent difference at 2.5 km

Figure 3.35: The left graph is the percent differences at 0.5 km for a series of misalignment plots with a lateral x-axis misalignment. The right graph is the percent differences at 2.5 km for a series of misalignment plots with a lateral x-axis misalignment.

For the case where the PMT was moved along the y-axis, upwards or downwards but remaining the same distance from the laser beam axis, the tolerance was approximately -2.2 mm to 2.2 mm. As with the previous misalignment the values of the overlap remain roughly constant with very little deviation from the ideal overlap within this range. Once the misalignment is outside the acceptable tolerance the overlap value decreases sharply. The two graphs in Figure 3.36 are the percent difference graphs corresponding to this misalignment.

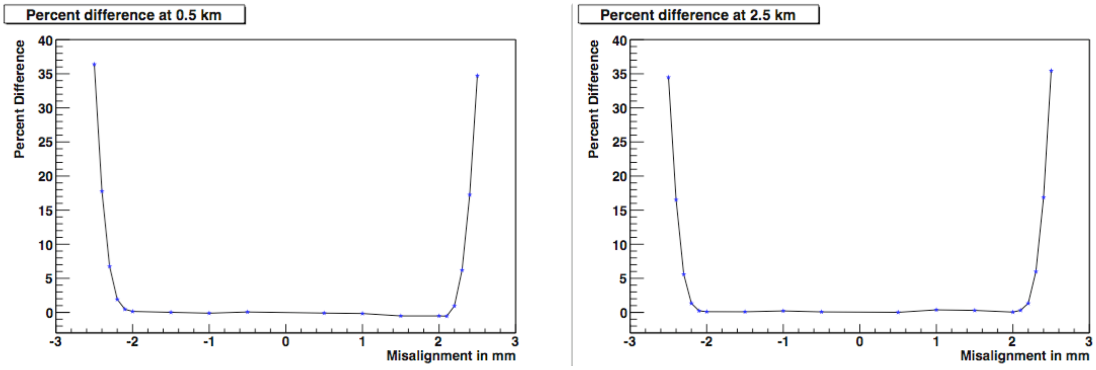

Figure 3.36: The left graph is the percent differences at 0.5 km for a series of misalignment plots with a lateral y-axis misalignment. The right graph is the percent differences at 2.5 km for a series of misalignment plots with a lateral y-axis misalignment.

For the case with a misalignment of the mirror in phi the tolerance was approximately -15 milliradians to 13 milliradians. As with the previous misalignments, the values of the overlap remain roughly constant with little deviation from the ideal overlap with in this range. Although more deviation from the ideal overlap is seen in this region as compared to misalignments of the PMT. As with the cases with a PMT misalignment once the misalignment is outside the acceptable tolerance the overlap value decreases sharply. The two graphs in Figure 3.37 are the percent difference graphs corresponding to this misalignment.

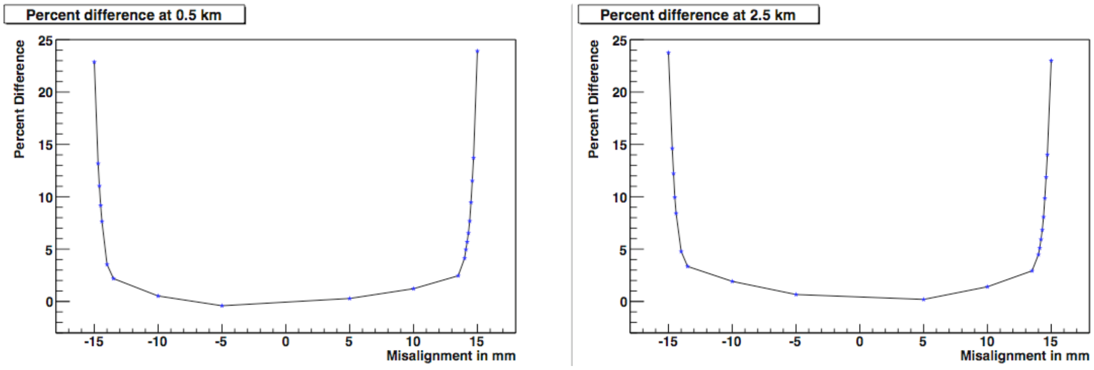

Figure 3.37: The left graph is the percent differences at 0.5 km for a series of misalignment plots with a misalignment in phi. The right graph is the percent differences at 2.5 km for a series of misalignment plots with a misalignment in phi.

For the case with a misalignment of the mirror in theta the tolerance was approximately -14 milliradians to 14 milliradians. As with the previous misalignments, the values of the overlap remain roughly constant with very little deviation from the ideal overlap with in this range. As with the phi misalignments more deviation is seen than in the cases with a misalignment of the PMT. Once the misalignment is outside the acceptable tolerance the overlap value decreases sharply. The two graphs in Figure 3.38 are the percent difference graphs for this misalignment.

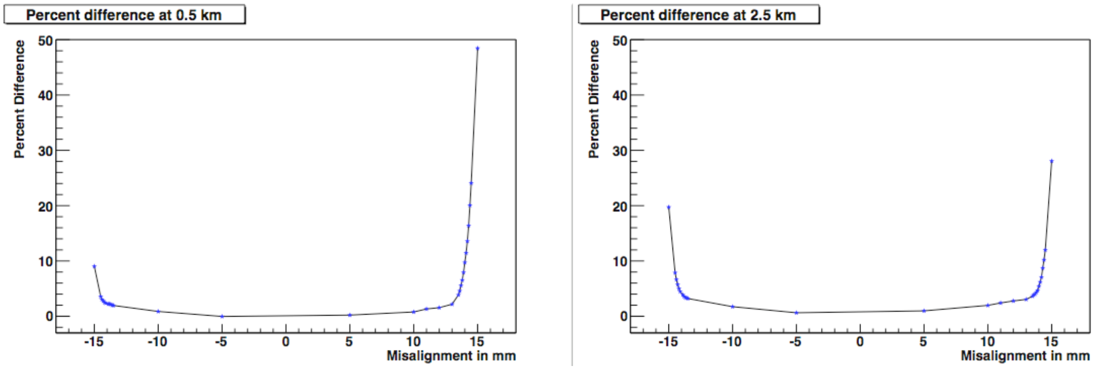

Figure 3.38: The left graph is the percent differences at 0.5 km for a series of misalignment plots with a misalignment in theta. The right graph is the percent differences at 2.5 km for a series of misalignment plots with a misalignment in theta.

As mentioned previously tables containing the exact tolerance ranges for each design are located in the appendix.

3.4 Lidar Prototype

From inspection of the overlap and S(*r*) function graphs, it is clear that the third design gives the greatest overlap. The first design had the second greatest overlap. However, the first design may not have the greatest stability while the lidar is in motion, due to the long PMT holder arms. The second version of the second design has the third greatest overlap and there is no noticeable difference between the first and third version of the second design. However, a 7.5 cm radius mirror was purchased prior to this study. Due to this, a design for the mirror and PMT support fashioned after the second version of second design will be used for the prototype. That is, the prototype is a mount that consists of a right cylinder with the mirror at one end and the PMT holder at the other end. The inside of the cylinder will be black to absorb backscattered light that strikes the interior wall. The arms to connect the PMT holder to the cylinder will be as small as possible but sturdy enough to maintain mechanical stability when the lidar system is in motion. This is the first prototype for the lidar upgrade; if after installation it is found that the smaller mirror gives too weak a signal then larger mirrors will be purchased and the third design, which is similar to the second version of the second design, will be used.

On 21 April 2009 the lidar prototype was successfully installed at the Coihueco fluorescence detector site.

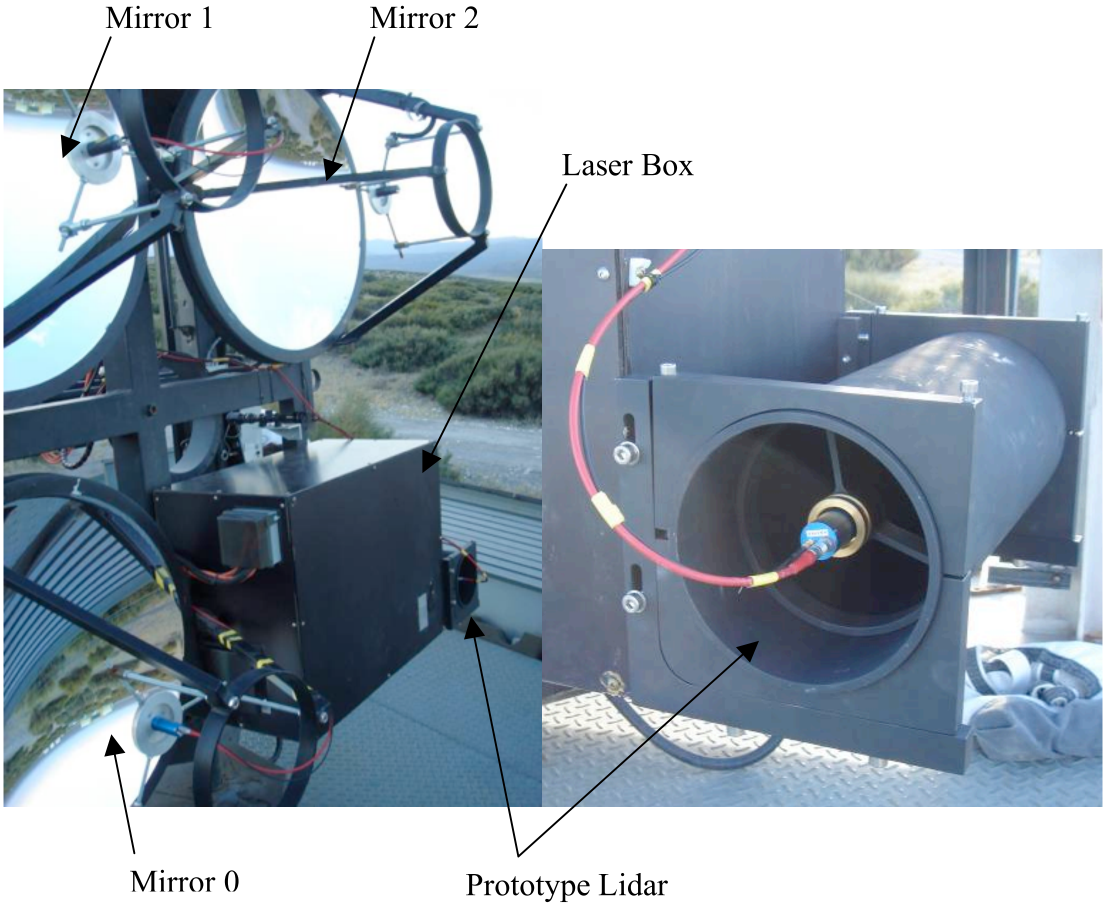

Figure 3.39: To the left is the whole lidar system including the prototype shown in the lower right of the image. To the right is the lidar prototype shown attached to the laser box.

The power from the prototype is compared to the power from Mirror 0 for a horizontal shot in Figure 3.40. From this plot one can see that in the near field the peak shown in the power is sharper for the prototype this in an early indication that the overlap for the prototype is improved, compared to the overlaps from the original system. This implies that the upgrade has better near field performance. The differing heights for the peaks are due to differences in the PMTs characteristics, such as the amount of background from detector noise.

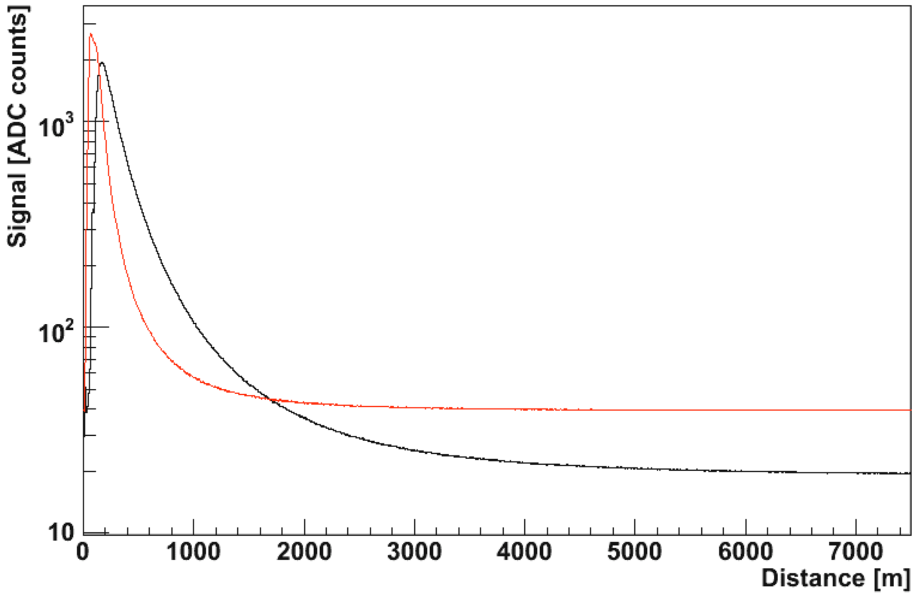

Figure 3.40: The power for the prototype, shown in red, and the power for Mirror 0, shown in black, plotted on a semi-log scale.

In Figure 3.41 an overlap plot for the prototype taken during the installation is shown and complete overlap is reached before 500 meters. In this plot the overlap reaches 1 due to the fact that the program that produced this plot normalizes the overlap. This is done in order to remove the effect of the pmt holder blocking a portion of the backscattered signal. The red vertical line in the plot marks the range at which the overlap has reached 95% of its maximum value.

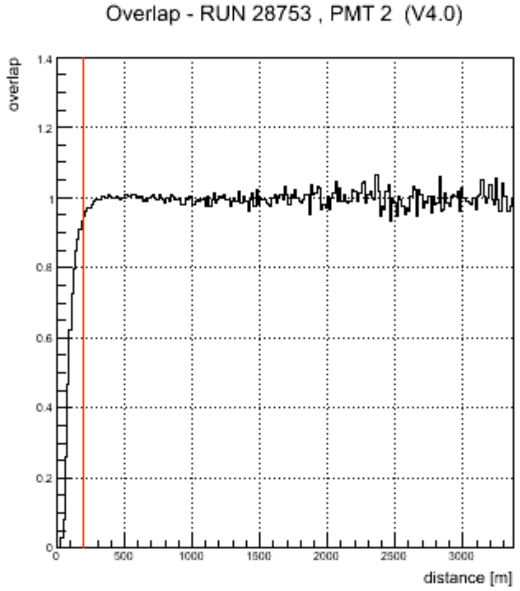

Figure 3.41: Overlap plot taken during installation of the prototype

3.5 Lidar Upgrade Final Design

Despite the success of the first prototype, several problems were found with the design during the installation, which needed to be addressed in the final design. To begin with it was found that alignment of the system was difficult with the current mounting design. The difficulties came from the weight of the prototype and the inability to tilt the system when aligning it with the laser beam axis. A second prototype has been designed with different mounting; the internal components are identical to the initial prototype design. The mounting for the second prototype was designed so that the lidar had both a pitch and yaw adjustment. This was done to allow the system to be tilled when aligning it with the laser beam. A model of the second prototype is shown in Figure 3.42.

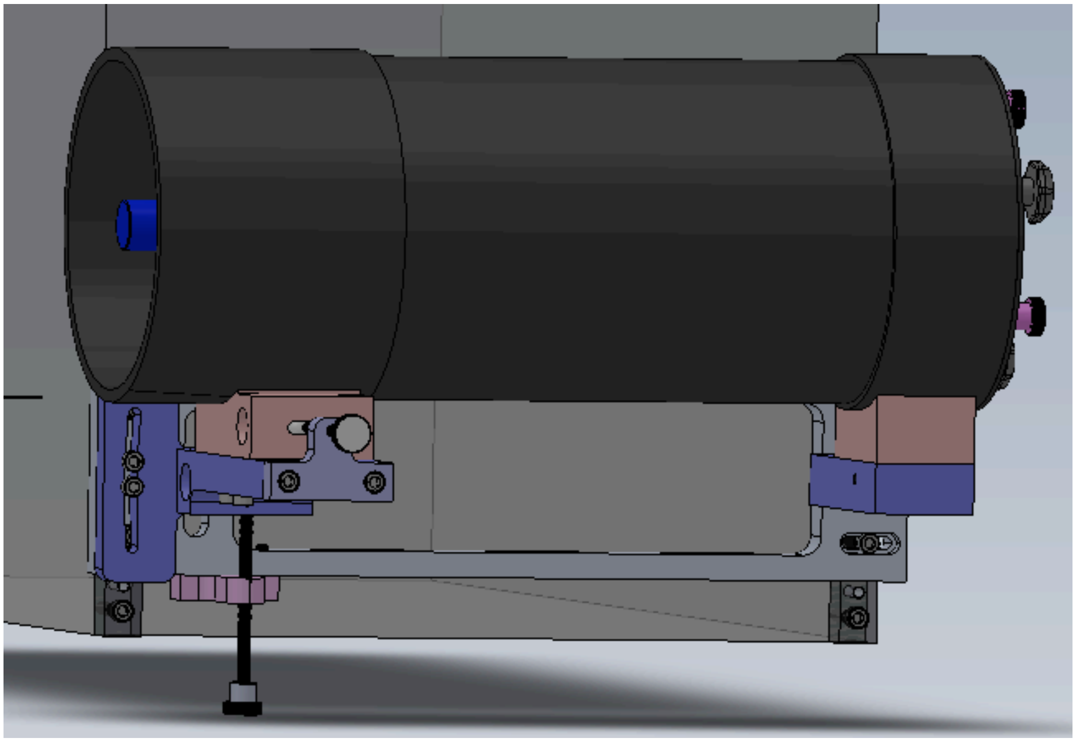

Figure 3.42: Second prototype model.

In addition to the difficulties with aligning the prototype the weight of the prototype was an issue. When mounting the first prototype, it was found that the frame needed to be counter balanced to prevent strain on the motor that moves the lidar mount. This was taken into account in the second lidar prototype and weight was removed wherever possible without jeopardizing structural integrity. This new mounting reduced the weight of the prototype by approximately half.

This second prototype was installed on 19 November 2009, replacing the first prototype at the Coihueco site.

Chapter 4
Conclusions And Future Work

The first prototype has shown that the addition of a small mirror to the current lidar system will improve the results for the lidar system in the near field. However, there is still work to be done before the near-field mirror can be added into the normal operations of all the lidar stations. The second near-field prototype will need to be studied over a period of time to insure that the system is stable and does not become misaligned over the course of normal lidar operation. Once the system is confirmed to be stable, the remaining three near-field mirrors will need to built and installed at the other lidar stations. After all of the near-field mirror have been added to the system the current lidar analysis software will need to be updated so that the signals from Mirrors 0 and 1 are accurately combined with the near-field mirrors signal. After these tasks are completed the upgrade to the Pierre Auger Observatory's lidar system will have a more accurate and complete view of the atmospheric conditions that affect cosmic ray detection.

Appendix

Original Lidar System Specifications

	Mirror 0	Mirror 1	Mirror 2
Mirror Radius (cm)	40	40	40
Focal Length (cm)	41	41	41
Transverse Offset (cm)	120	170	120
PMT Holder Radius (cm)	6	6	6
PMT Height (cm)	6.1	6.1	6.1

Design Tolerance Tables

Design Tolerances for the Lateral Displacement the PMT along the x-axis in millimeters

	0.2 km	0.5 km	1.0 km	2.5 km
Design 1	-2.3 – 1.8	-2.2 – 2.1	-2.2 – 2.1	-2.2 – 2.1
Design 2 v1	-2.4 – 2.0	-2.3 – 2.1	-2.3 – 2.2	-2.3 – 2.2
Design 2 v2	-2.4 – 2.0	-2.3 – 2.1	-2.3 – 2.2	-2.3 – 2.2
Design 2 v3	-2.4 – 2.0	-2.3 – 2.2	-2.3 – 2.2	-2.3 – 2.2
Design 3	-2.0 – 1.5	-2.0 – 1.5	-2.0 – 1.5	-1.5 – 1.5

Design Tolerances for the Lateral Displacement the PMT along the y-axis in millimeters

	0.2 km	0.5 km	1.0 km	2.5 km
Design 1	-2.2 – 2.2	-2.2 – 2.2	-2.2 – 2.2	-2.2 – 2.2
Design 2 v1	-2.2 – 2.2	-2.2 – 2.2	-2.2 – 2.2	-2.2 – 2.2
Design 2 v2	-2.2 – 2.2	-2.2 – 2.2	-2.2 – 2.2	-2.2 – 2.2
Design 2 v3	-2.2 – 2.2	-2.2 – 2.2	-2.2 – 2.2	-2.2 – 2.2
Design 3	-1.7 – 1.7	-1.8 – 1.7	-1.8 – 1.8	-1.8 – 1.8

Design Tolerances for the Theta Adjustment of the Mirror in milliradians

	0.2 km	0.5 km	1.0 km	2.5 km
Design 1	-15.0 -12.0	-14.5 – 13.5	-14.0 – 14.0	-14.0 – 14.0
Design 2 v1	-15.0 -11.0	-14.5 – 13.5	-14.0 – 13.0	-14.0 – 13.5
Design 2 v2	-15.0 -12.0	-14.5 – 13.5	-14.0 – 13.5	-14.0 – 14.0
Design 2 v3	-15.0 – 12.0	-14.0 – 13.0	-14.0 – 14.0	-14.0 – 14.0
Design 3	-13.5 – 11.0	-13.0 – 11.5	-13.0 – 12.0	-13.0 – 12.5

Design Tolerances for the Phi Adjustment of the Mirror in milliradians

	0.2 km	0.5 km	1.0 km	2.5 km
Design 1	-12.0 – 14.0	-13.5 – 14.0	-13.5 – 14.0	-13.5 – 14.0
Design 2 v1	-14.0 – 14.0	-14.0 – 14.0	-14.0 – 14.0	-14.0 – 14.0
Design 2 v2	-14.0 – 14.0	-14.0 – 14.0	-14.0 – 14.0	-14.0 – 14.0
Design 2 v3	-14.0 – 14.0	-14.0 – 14.0	-14.0 – 14.0	-14.0 – 14.0
Design 3	-12.0 – 12.0	-12.5 – 12.0	-12.5 – 12.5	-12.5 – 12.5

References

[1] S.Y. BenZvi, et al., *The Calibration and Optimization of the Auger Elastic Lidar System*, Pierre Auger Note: GAP-2007-033.

[2] S.Y. BenZvi, et al., *The Lidar System of the Pierre Auger Observatory*, Nucl. Instr. Meth. **A 574** (2007) 174.

[3] R. Cester, et al., *Atmospheric aerosol monitoring at the Pierre Auger Observatory*, in Proc. 29th Int. Cosmic Ray Conference, Pune, India, (2005), **8**, 347-350.

[4] R. Clay, B. Dawson, *Cosmic Bullets*, Helix Books, 1997.

[5] B. Fick, et al., *The First Central Laser Facility*, Pierre Auger Note: GAP-2004-003.

[6] M. W. Friedlander, *A Thin Cosmic Rain*, Harvard University Press, 2000.

[7] J. Harms, et al., *Geometrical compression of lidar return signals*, Applied Optics, **17** (1978).

[8] V. A. Kovalev and W. E. Eichinger, *Elastic Lidar Theory, Practice, and Analysis Methods*, Wiley ed., 2004.

[9] G. Matthiae, *Optics and Mechanics of the Auger Fluorescence Detector*, Pierre Auger Note: GAP-2001-037.

[10] The Pierre Auger Collaboration, *Correlation of the Highest-Energy Cosmic Rays with Nearby Extragalactic Objects*, Science **318**, 938, (2007).

[11] The Pierre Auger Collaboration, *Official website*, http://www.auger.org/.

[12] The Pierre Auger Collaboration, *The Pierre Auger Northern Observatory Design Report*, 2009.

[13] The Pierre Auger Collaboration, *The Pierre Auger Project Design Report*, 1996.

[14] M.V.S Rao and B.V. Sreekantan, *Extensive Air Showers*, World Scientific Publishing, 1998.

[15] G. Sequerios, *Lidar Technique for Atmospheric Monitoring in the Pierre Auger Observatory*, Ph.D. Thesis, (2006).

[16] P. Sokolsky, *Introduction to Ultrahigh Energy Cosmic Ray Physics*, Westview Press, 2004.

[17] A. S. Tonachini, *Atmospheric Calibration of the Fluorescence Detectors with the LIDAR System of the Pierre Auger Observatory*, Ph.D. Thesis, (2007).

[18] C.T.R. Wilson, *On the Spontaneous Ionisation of Gases*, Roy. Soc. Proc. **69** (1901) pp. 277-282.